CIMAT Centro de Investigación en Matemáticas, A.C.

CHARACTERIZING THE ERROR OF THE GAUSSIAN PROFILE TO MODEL AXON BUNDLES DIFFUSIVITY

T E S I S

Que para obtener el grado de

Maestro en Ciencias

con Especialidad en

Computación y Matemáticas Industriales

Presenta

Alfonso Rojas Oaxaca

Directores de Tesis:

Dr. Alonso Ramírez Manzanares

Dr. José Luis Marroquín Zaleta

Autorización de la versión final

Guanajuato, Gto., 8 de Noviembre de 2019

CENTRO DE INVESTIGACIÓN EN MATEMÁTICAS

MASTERS THESIS

Characterizing The Error Of The Gaussian Profile To Model Axon Bundles Diffusivity

Author:
Alfonso ROJAS-OAXACA

Supervisors:
Alonso
RAMÍREZ-MANZANARES

José Luis
MARROQUIN-ZALETA

A thesis submitted in fulfillment of the requirements
for the degree of Master of Science in Computer Science and Industrial Mathematics

in the

Department of Computer Science

CIMAT

November 8, 2019

Declaration of Authorship

I, Alfonso ROJAS-OAXACA, declare that this thesis titled, "Characterizing The Error Of The Gaussian Profile To Model Axon Bundles Diffusivity" and the work presented in it are my own. I confirm that:

- This work was done wholly or mainly while in candidature for a research degree at this University.
- Where any part of this thesis has previously been submitted for a degree or any other qualification at this University or any other institution, this has been clearly stated.
- Where I have consulted the published work of others, this is always clearly attributed.
- Where I have quoted from the work of others, the source is always given. With the exception of such quotations, this thesis is entirely my own work.
- I have acknowledged all main sources of help.
- Where the thesis is based on work done by myself jointly with others, I have made clear exactly what was done by others and what I have contributed myself.

Signed:

Date:

"Everything should be as simple as it can be, but not simpler."

Albert Einstein

CENTRO DE INVESTIGACIÓN EN MATEMÁTICAS

Abstract

Department of Computer Science

Master of Science in Computer Science and Industrial Mathematics

Characterizing The Error Of The Gaussian Profile To Model Axon Bundles Diffusivity

by Alfonso ROJAS-OAXACA

Diffusion Tensor Imaging (DTI) is one of the most widespread techniques for obtaining information about the underlying tissue geometry and integrity in brain white matter. Despite its limitations and strong assumptions, it is a robust model, widely used in clinical applications. Some examples include the detection of Ischemia; the study of alteration produced by conditions, such as Multiple Sclerosis and Alzheimer's. Two important limitations of DTI are the impossibility of describing diffusion in substrates with separations and compartments, and the high count of degrees of freedom. Nevertheless, the model can be expanded to represent the signal as the sum of contributions from different tensors; the multi tensor model. Also, some constraints can be assumed to decrease the number of free parameters.

In this thesis work, we test constrained multi tensor models (i.e Zeppelin and Stick) through Montecarlo simulations in order to gain some insights on the limits of assuming Gaussian diffusion in the description of neuroanatomy. Montecarlo simulation of the diffusion process is performed in several substrates, which resemble white matter microstructure. Physical parameters are obtained by fitting multi tensor models in one fiber bundle, and crossings of two bundles. The MRI signal obtained by the simulator is free of noise and artifacts to factor out any other source of variability, besides the stochastic simulation itself. Finally, the fitted parameters of the model are compared to the statistics of the spin trajectories of the simulator.

We observe low errors in the case of extracellular compartment diffusion. In the case of a single complete bundle, simple Zeppelin diffusion underestimation worsens as the volume fraction increases. Zeppelin + Stick model improves quality substantially, with deviation also increasing proportional to volume fraction. Rotation angle does not seem to play an important role in the estimation error. In the crossing case, the use of multiple shells reduces error substantially.

Acknowledgements

Primordialmente, a quienes debo de agradecer es a mi familia, quienes me han dado todo el apoyo del mundo, y hasta más. Quiero agradecer a mi mamá, que básicamente es es quién me ha empujado (a veces de forma un poquito demasiado literal) a ser quien soy hoy. A mi papá, que considero a una de las personas más sabias que conozco, y que suele pasarme un poquito de su sabiduría. A la vaca por sus memes, apoyo emocional y psicológico. Al gordo por acompañarme en tiempos difíciles y pasarme música chida. A mi abuelita Lupe por venirme a cuidar y contarme sus historias y secretos. A mis tíos y primos por cuidar de mi familia y papá cuando estaba enfermo. A a mi abuelo Nacho, mi abuela Guillermina, y a mi tío Memo, que desafortunadamente no pudieron leer esto.

Dicen que no debes de agradecer en tu tesis a tu actual pareja por si las cosas acaban feo, pero el omitir todo el apoyo y el amor de Sab sería un crimen (ya ahí le vendré a echar corrector si cortamos). Quiero agradecer también el apoyo que me dieron mis amigos más cercanos. A Álvaro por rescatarme de mi miseria de foráneo con anécdotas electrosatánicas. Al Renato por hospedarme y acompañarme en mis technoaventuras. A Ariel por obligarme a aprender a programar bien. A Dahlia por enviarme cabras esporádicas y por ayudarme a acabar la licenciatura prestándome lapiceros. A David por ser mi confidente ocasional (extraño las navecitas). A Diana por los libros y las fiestas cervantinas. Al Jaime por ayudarme con el PoncoFest 2018, y la demás bandita cricka por los buenos momentos (aunque nunca me vineron a visitar los hp's). A los *cubies* y compas que conocí en CIMAT, así como a quien se me olvide (o no?) poner.

También, por supuesto, está todo el apoyo intelectual para el desarrollo de este trabajo. Quiero agradecer al Dr. Alonso, quien me apoyó en demasiadas cosas como para listar cada una de ellas, desde el desarrollo de la linea de investigación hasta consejos de mi propia carrera profesional. Al Dr. José Luis por sus muy acertadas observaciones e ideas, que evitaron que la tesis perdiera el enfoque. Al Dr. Arturo Gonzáles de la Universidad de Guanajuato por contribuir con feedback como colaborador. También agradezco a todos los profesores que me han apoyado a lo largo de toda mi carrera, como el Profesor Adolfo Arias de la primaria; profe José Gómez de la secundaria; profe Ulises del Morál y profa de la prepa; Dr. Roberto Rosas y Dr. Gibrán Etcheverry de UDLAP; Dr. José Martinez y Dr. Felipe Orihuela de INAOE; todos mis maestros en CIMAT y quienes se me haya pasado poner.

Este trabajo fue realizado gracias al apoyo económico del programa de becas nacionales del CONACyT.

Contents

List of Figures

List of Tables

List of Abbreviations

DTI	**D**ifussion **T**ensor **I**maging
DPD	**D**iscrete **P**robability **D**istribution
DDPD	**D**iscrete **P**robability **D**ensity **D**istribution
EAP	**E**nsemble **A**verage **P**ropagator
ICVF	**I**ntra **C**ellular **V**olume **F**raction
KLD	**K**ullback **L**iebler **D**ivergence
PGSE	**P**ulsed **G**radient **S**pin **E**cho

List of Symbols

b	b-value	$\mathrm{s\,m^{-2}}$
B	magnetic field intensity	T
$D, \boldsymbol{D}$	diffusion coefficient/tensor	$\mathrm{m^2\,s^{-1}}$
f	Volume Fraction	
$\boldsymbol{g}$	normalized gradient direction	
L	diffusion length	m
$\boldsymbol{H}, \boldsymbol{h}$	DPD from simulator	
$\boldsymbol{q}$	wavevector	$\mathrm{m^{-1}}$
$\boldsymbol{r}$	position vector	m
α	mixing factor between two crossing fiber bundles	
γ	gyromagnetic ratio	$\mathrm{rad\,s^{-1}\,T^{-1}}$
Δ	diffusion time/separation between PGSE gradients	s
θ	parametrized angle of crossing between fibers	rad
ω_P	Larmor precession frequency	$\mathrm{rad\,s^{-1}}$

Para los que se fueron.
Para los que están.
Para los que llegarán.
Pero sobre todo…
Para los que siempre han estado.
¡Gracias por todo, Chojemas!

Chapter 1

Introduction

1.1 Motivation

Connectomics, also called Brain Hodology, is the study of anatomy of the communication pathways between regions of the brain which are relatively far away from each other. Connectomics main goal is the production and study of extensive and complex maps of neural circuits formed by function-related neurons connected by synapses. Neurons reach to other distant neurons using elongations of its cellular body called axons. Axons are very large compared to the neuron body size. Most neurons exist in the cortex, so electrical signals must travel between zones of the cortex, sometimes even across brain hemispheres. The zones of the brain which are mainly composed of these groups of axons are called white matter.

The white matter is a tissue which constitutes approximately half of the total volume of the brain (Jones, 2010). It is conformed by bundles of myelinated axons called nerve tracts. The function of this tissue is to relay signals generated and processed by neurons, in the form of action potentials. It used to be considered an uninteresting, passive tissue existing solely as the support of the gray matter. Now, it is know that white matter plays a fundamental role on the neural inner workings, and it's study is of great importance for our clinical and functional knowledge of the brain (Irimia et al., 2012). There are more than 100 known disorders in which a white matter alterations are the predominant or unique factor involved. All of these disorders affect negatively the emotional and cognitive function of the affected person (Filley, 2012). Because of this, Connectiomics plays a fundamental role in our understanding of the brain.

The brain complexity is overwhelming. The human cortex, which constitutes 82% of the total mass of the brain, has around 16 billion neurons (Herculano-Houzel, 2009). Because of this, Connectomics has to study the brain at different scales. In this work, we are focused on the main tool used to produce macroscale connectomes, which is Diffusion-Weighted Nuclear Magnetic Resonance Imaging. More precisely, we are centered on some of the mathematical models used to translate the signals obtained by an MRI machine to real physical measurements of the microstructure of white matter.

1.2 Objective

Magnetic Resonance Imaging with Diffusion Weighted Imaging (MRI-DWI) measures the natural diffusive movement of water molecules inside the brain. Their displacement is dictated by the surrounding medium. The medium inside the brain is not plain water, as the molecules are restricted by the myelin sheaths of the axons, the walls of the

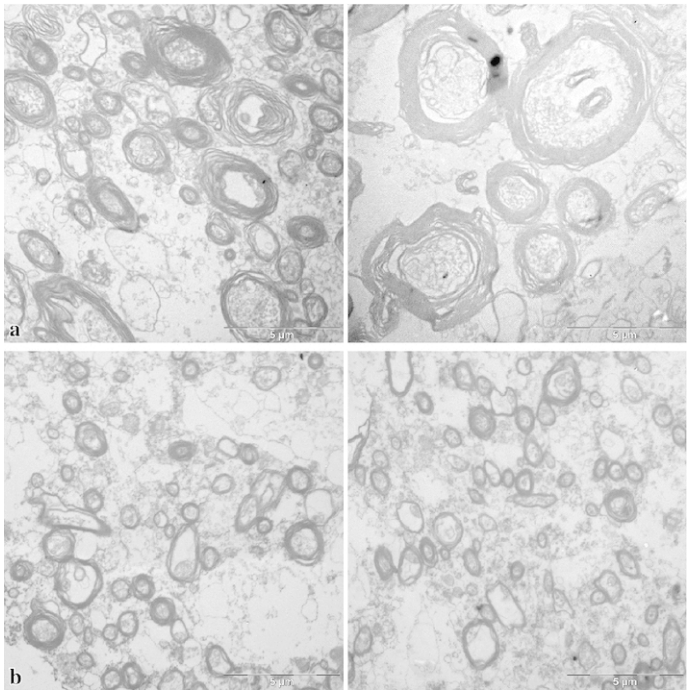

FIGURE 1.1: Electron micrographs from a human brain's White Matter, a) from the superior longitudinal fascicle, b) from the uncinate/inferior occipitofrontal fascicle. Left) left hemisphere, right) right hemisphere. Adapted from Liewald et al., 2014.

nerve tracts, the cellular membranes, intra-cellular organelles and such. Because of this, the information of water diffusion can be used to obtain insights about the underlying microstructure of the brain, such as the fiber orientation, the intra-axonal volume ratio, and the radii distribution of the axons. Nonetheless, the process of correlating the measures of the MRI device to these features is not trivial. In the first place, the acquisition process introduces noise, artifacts and other sources of variance inherent in measuring a live subject or patient. Even if engineers could solve all the limitations of technology, the fundamental inverse problem remains. Given an MRI-DWI signal (in this case, perfect), what are the causal factors that produced it? In this case, how the underlying microstructure, which shapes the water diffusion inside the brain, looks like? To answer this question, a plethora of models have been proposed. These models of the diffusion process vary in complexity and number of parameters (Ferizi, Schneider, Witzel, et al., 2015).

As any abstraction of a complex physical process, choosing a right model is a trade off between simplicity and accuracy (Aragones et al., 2002). A model with more parameters could explain the process better, but become unstable and too sensitive to noise. On the other hand, what a simpler model might lack in detail about the intricacies of the phenomenon, it could compensate it in being more resilient, and have better accuracy on the fewer parameters that predicts. For that reason, we characterize a simple and widely used model; which is the diffusion tensor. More precisely, this work focuses on special cases of the former, which characterize diffusion along a bundle of axons, and

perpendicular to that directions. We also analyze a simple bi-compartment case to take into account the water trapped inside the axons. Finally, we explore the case of a simple crossing of two bundles of axons by fitting a per-bundle, intra-voxel, restricted diffusion tensor.

The diffusion tensor model is simple, but makes strong assumptions about the nature of the substrate in which water diffuses. So, the main interest of this work is to quantify the bias of the model parameters against the real process, which does not necessarily meet the conditions assumed by the model.

1.3 Summary

After this introduction, the next Chapter will introduce succinctly the physics behind the diffusion process, how it is affected by the microstructure of the brain, and how the Diffusion Tensor came to be. The third will present the theory of Diffusion-Weighted Magnetic Resonance Imaging (DW-MRI), the obstacles in real life, and a discussion on the limitations of the Diffusion Tensor. The fourth Chapter describes the materials and methods we used to try to quantify the error between fitted models and the diffusion inside various known, synthetic substrates using Montecarlo simulation. Finally, the last two Chapters present our results in model fitting and our conclusions derived from these experiments.

Chapter 2

Diffusion Inside The Brain

Diffusion refers to the net movement of matter from a region of a system to other, from a zone of higher concentration to another with less concentration. This process is the result of the erratic movement of atoms or molecules as result of the thermal energy and collisions between them, a phenomenon known as Brownian motion, in honor of Robert Brown (Brown, 1828). A liquid medium, such as inside the brain, is composed of an immense amount of molecules moving by diffusion, or by blood flow. The movement of water is modulated by obstacles such as membranes with varying degrees of permeability, myelin sheaths, and such. In the next section, the physical models describing the behavior of the diffusive movement are explained in further detail.

2.1 Physical Model

One should note that there is no direct underlying force pushing the molecules in the negative direction of the concentration gradient, as diffusion is merely the macroscopic manifestation of the statistical trend of the particle ensemble (a thermodynamic system) to maximize its entropy. The apparent force behind this movement is called an entropic force (Roos, 2014). The macroscopical behavior of this process was described by Frick.

2.1.1 Frick's Laws

Diffusion is quantified as flux, which is a vector whose units are $quantity/(time \cdot area)$. Frick laws describe the vector flux $\boldsymbol{J}(\boldsymbol{r})$ of a quantity of matter through an infinitesimal area in certain point $\boldsymbol{r}$ at an instant t,

$$\boldsymbol{J} = -D\nabla_{\boldsymbol{r}} n(\boldsymbol{r}, t) \tag{2.1}$$

$$\frac{\partial n(\boldsymbol{r}, t)}{\partial t} = D\nabla_{\boldsymbol{r}}^2 n(\boldsymbol{r}, t), \tag{2.2}$$

where $n(\boldsymbol{r}, t)$ is the concentration of solute particles in $\boldsymbol{r}$ at time t, ∇ is the gradient operator, and $\nabla^2 = \nabla \cdot \nabla$ is the Laplacian. D is the diffusion coefficient.

2.1.2 Einstein Formulation

These laws were originally formulated taking a macroscopic concentration gradient into account, but they can also be applied in the case of self-diffusion in the absence of one. Einstein took the concentration of a particle as the probability of finding a molecule.

He inferred this probability in a medium with no macroscopic concentration gradient should be macroscopically uniform, but locally structured due to Brownian Motion. He rewrote the Frick equations using the notion that solute particles in a liquid behave like an ideal gas. He did it in terms of diffusion under a probabilistic gradient (Einstein et al., 1905).

Let $P(\boldsymbol{r}_0|\boldsymbol{r}', t)$ be the probability density function of a particle walking from $\boldsymbol{r}_0$ to $\boldsymbol{r}'$ in time t:

$$\frac{\partial P(\boldsymbol{r}_0|\boldsymbol{r}', t)}{\partial t} = D\nabla^2 P(\boldsymbol{r}|\boldsymbol{r}', t). \tag{2.3}$$

The conditional probability $P(\boldsymbol{r}_0|\boldsymbol{r}', t)$ is called the diffusion propagator. This reformulation describes Brownian motion as a stochastic process in which probability densities obey differential equations. A statistical ensemble is defined as a set of a very large (sometimes infinite) number of copies of a system, where each one represents a state the system may be in (Gibbs, 2014). Considering all of the possible states S a system might take, this can be considered as the probability distribution of the state of a system. In free autodiffusion, the propagator is independent of the starting point and can be applied to the ensemble of all possible trajectories of a particle. It is possible then to simplify the notation in terms of displacement vectors $\bar{\boldsymbol{r}} = \boldsymbol{r}' - \boldsymbol{r}_0$ (or considering the initial condition of the system being $\boldsymbol{r}_0 = \boldsymbol{0}$ for all particles):

$$\frac{\partial P(\bar{\boldsymbol{r}}, t)}{\partial t} = D\nabla^2 P(\bar{\boldsymbol{r}}, t). \tag{2.4}$$

By solving (2.4) using the aforementioned initial condition, and assuming the absence of obstacles that could interfere with the free diffusion of molecules, leads to a Gaussian density form,

$$P(\boldsymbol{r}, t) = \frac{1}{\sqrt{(2\pi\Sigma)^3}} \exp(-\frac{1}{2\Sigma}\bar{\boldsymbol{r}}^T\bar{\boldsymbol{r}}), \tag{2.5}$$

where $\Sigma = 2tD$.

The average of a given property A of the ensemble is defined as

$$\langle A \rangle := \sum_{s \in S} P(s)A(s). \tag{2.6}$$

Using this concept, the mean square displacement of the molecules can be computed, taking into account the Gaussian nature of the distribution. This leads to the identity known as Einstein-Smoluchowski relation for diffusion. For the n-dimensional case is (Dill and Bromberg, 2012)

$$\langle (\boldsymbol{r}' - \boldsymbol{r}_0)^2 \rangle = \langle \bar{\boldsymbol{r}}^2 \rangle = 2nD\Delta. \tag{2.7}$$

Here, Δ has the same use as t. However, there is a conceptual difference. We call Δ the diffusion time of our experiment, so the experiment ends at the instant $t = \Delta$.

2.1.3 Anisotropy

All this reasoning was done assuming an homogeneous, isotropic substrate, which means the Apparent Diffusion Coefficient is the same in any part of the substrate, and

in any direction. However, the later case is not valid when the substrate diffusivity changes in function of the chosen direction. So, we generalize (2.3) to change the shape of the diffusion propagator depending on the direction. The Diffusion Tensor $\boldsymbol{D}(\boldsymbol{r})$ describes how the particle flux is related to the temporal derivative of the Diffusion Propagator at any starting point $\boldsymbol{r}$. Generally, a Cartesian frame of reference can be found where $\boldsymbol{D}$ is diagonal. For the 3-dimensional case, the tensor has the form

$$\boldsymbol{D} = \begin{pmatrix} D_x & 0 & 0 \\ 0 & D_y & 0 \\ 0 & 0 & D_z \end{pmatrix}. \tag{2.8}$$

Of course, the tensor can be rotated to any frame, where all the elements of the matrix might be greater than zero. Thus, (2.3) is expanded to account for anisotropy and heterogeneity.

$$\frac{\partial P(\boldsymbol{r}_0|\boldsymbol{r}', t)}{\partial t} = \nabla_{\boldsymbol{r}'} \cdot [\boldsymbol{D}(\boldsymbol{r}') \nabla_{\boldsymbol{r}'} P(\boldsymbol{r}_0|\boldsymbol{r}', t)]. \tag{2.9}$$

In the special case where diffusion is Gaussian and anisotropic, the propagator has the following form (Price, 1997):

$$p(\bar{\boldsymbol{r}}, \Delta) = (4\pi\Delta)^3 (\sqrt{\det \boldsymbol{D}}) \exp\left(\frac{-\bar{\boldsymbol{r}}^T \boldsymbol{D}^{-1} \bar{\boldsymbol{r}}}{4\Delta}\right). \tag{2.10}$$

2.2 Neuroanatomy for diffusion: a crash course

The Central Nervous System (CNS) is essentially built around neuronal cells interconnected to each other through axons, which function as transmission lines for electrical action potentials. Such axons can reach distant neuroanatomical regions. Bundles of axons interconnect clusters of neurons with similar functions. Gray matter, which is compromised mostly of neuron bodies and short range interconnections, the measured diffusivity, diffusion is largely isotropic, independent of the measuring direction, so a single scalar can describe the diffusion profile. In contrast; the diffusion in structurally oriented media, such as in the nerve tracts of white matter, is anisotropic. Water can move freely along the fiber orientation, but is restricted by the axon walls to move perpendicular to it, meaning the diffusion is dependent on the direction (Moseley et al., 1990) (Henkelman et al., 1994).

2.2.1 What can be found inside White Matter?

The human brain is one of the most complex objects known. Its intricacies and functions are still being discovered. Several structures and cells have been found and characterized using microscopy techniques. The brain can be divided in two types of tissue which can be macroscopically differentiated, the gray and white matter. Gray matter is mainly made of neurons, unmyelinated axons and glial cells. White matter is formed by myelinated axons grouped in nerve tracts, oligodendrocytes and also glial cells. Glial cells are divided in microglia and macroglia. Some cells that can be found in the white matter, and that may influence water diffusion, are:

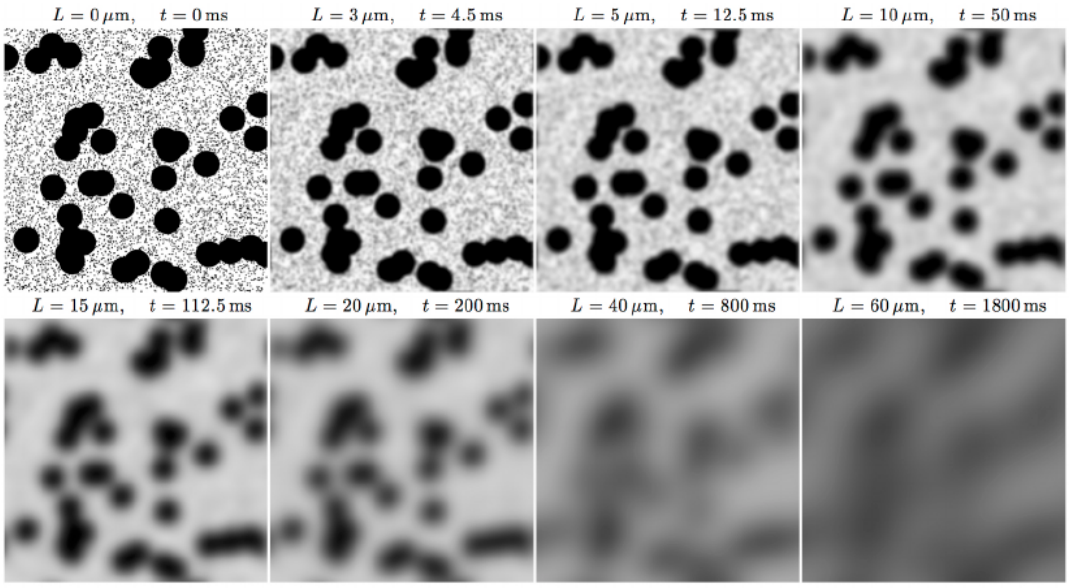

FIGURE 2.1: Simulation of how the substrate is *seen* by the diffusing molecules. Novikov et al. used a Gaussian filter with a bandwidth of $L/2$ to represent the coarse graining that occurs when the timescale changes. Adapted from Novikov, Fieremans, et al., 2019.

- Oligodendrocytes, which produce the myelin sheath of the axons and support axonal structure.
- Astrocytes, which play numerous supporting roles, such as metabolic support and ion concentration regulation.
- NG2-positive cells, being the precursors of the former glia.
- Microglia small phagotic cells part of the inmunne system.
- Ependymal, endothelial, pericytes and fibroblasts cells make the vascular system inside the brain.

For more details on the anatomy of white matter, refer to Edgar and Griffiths, 2014.

2.2.2 Coarse to fine

One can see from (2.5) that the shape of the diffusion propagator in heterogeneous media depends of the starting point $\mathbf{r}$, and diffusion time. This happens because the average diffusion length $L = \sqrt{2D\Delta}$, which comes from the Einstein equation, is dependent of time. A good intuitive example of the scale dependence of the diffusion parameters can be found on Figure 2.1 taken from Novikov, Fieremans, et al., 2019. Imagine a 2D substrate with a known diffusion coefficient D_0. The substrate has randomly distributed disks of two different radius; a small radius and a big radius, 20 times larger than the small. At the beginning, the molecules only react to their immediate local environment, so the apparent diffusion coefficient is $D|_{t=0} = D_0$. After some small lapse of time,

the molecules are mostly hindered by the smaller disks. If we let more time pass, long enough for the diffusion length to widely surpass the small disk size, their microscopic effect will become averaged, and diffusion would look as if only the larger disks remain, and the diffusion coefficient of the medium decreased. If we were unable to look at the shorter diffusion time, it would be impossible to know the existence of the smaller disks. After a longer time, the contribution of all the microstructure becomes coarse-grained, and the measure would look as if it came from a uniform isotropic medium with an even smaller global diffusion coefficient. This is the reason MRI measures *apparent* diffusion coefficients, because they vary depending on how much time the spins have to interact with their surroundings.

2.3 Fiber tracts: the main contributor to diffusion anisotropy

The complete biophysics of diffusion anisotropy in brain tissue are not completely understood currently. Most researchers ascribe it to ordered, heterogeneous structure, such as oriented macromolecules, supramolecular structures, organelles and membranes. This section lists briefly the known relevant effects on diffusivity caused by the inner microstructure of the human brain. For a much more in-depth review of how neuroanatomy affects diffusion, refer to Beaulieu, 2002; Beaulieu, 2014.

The axonal cytoeskeleton is made of actin filaments, microtubule-associated proteins and neurofilaments (Nixon, 1998). Neurofilaments provide structure and are the mains determinant of the diameter of the fibre. Both neurofilaments and microtubules lie parallel to the direction of the axon. The intra-axonal cytoplasm contains organelles such as mitochondria, multivesicular bodies, endosomes, lysosomes, vesicles and axoplasmic reticulum. Mitochondria can move along the microtubules, and Non-myelinated and dysmyelinated axons tend to have a higher density of them (Campbell, Smith, and Mahad, 2012). The axon diameter remains relatively constant throughout the axon's length (Friede and Samorajski, 1970). In the CNS, the majority of axons greater than 0.2 µm in diameter are myelinated (Hirano and Llena, 2009). Axonal packing densities are influenced by axonal diameters and the proportion of axons that are myelinated. Consequently, densities can vary greatly from one white matter tract to another. Myelin is the membranous, lipid-rich structure generated by the compaction of concentric lamellae of individual oligodendrocyte processes around an axonal segment. Myelin increases the rate of electrical conduction of an axon of a given diameter by 10 to 100 times (Trapp and Kidd, 2004). The myelin sheath is not continuous along the length of the axon. It is interrupted at regular distances by small unmyelinated regions called nodes of Ranvier. The axon and the oligodendrocyte are intimately related and interdependent. The proliferation of one means the proliferation of the other.

2.3.1 Quantifying anisotropy

The water diffusion along to the fiber is subject to less restriction than across it, because of membranes and myelin wrapping. As will be detailed in Chapter 3, it is possible to infer the diffusion tensor under some assumptions. The mean diffusivity (MD) is defined as the average of the tensor's eigenvalues, or one third of the trace of the matrix (Basser and Pierpaoli, 1996). This is a measure of the bulk diffusivity without considering diffusion direction. The tensor's greatest eigenvalue λ_1 corresponds to the apparent

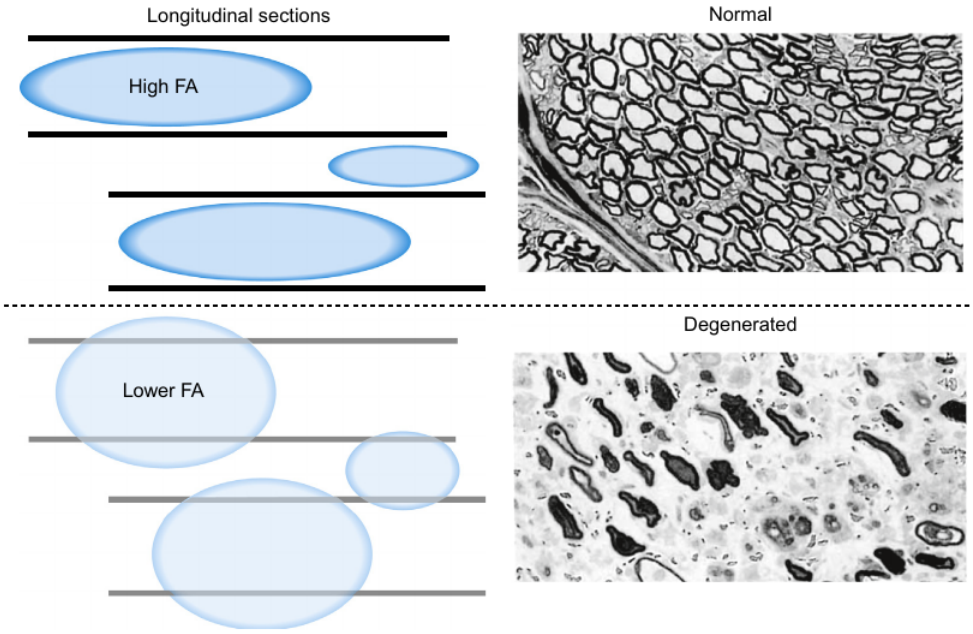

FIGURE 2.2: Cartoon illustrating that structural damage to axons and myelin that result in alterations to the directional barriers of water diffusion will reduce the degree of anisotropy. Adapted from Johansen-Berg and Behrens, 2013.

diffusion coefficient in the direction with less restriction, i.e. the parallel diffusivity $D_{\parallel}$ to the fiber. This, of course, assumes the case of regions of the human brain with no crossing fibers. Because of the properties of the diffusion tensor, the other eigenvectors are orthogonal to the parallel direction. If we assume radial symmetry, $\lambda_2 = \lambda_3$. This is called the radial, or orthogonal diffusivity $D_{\perp}$. The degree of anisotropy is defined as the deviation between $D_{\perp}$ and $D_{\parallel}$. There are different anisotropy measures, being Fractional Anisotropy (FA) (Basser and Pierpaoli, 1996) the most used in DTI studies.

2.3.2 Anisotropy and White Matter tissue microstrucutre

The ordered axonal architecture is thought to be the main factor behind directionality and anisotropy on the diffusion of water. Most of the nerve tracts in white matter are aligned in parallel. They may me coherently directed in one direction, such in the optic nerve relaying signals from the eye, or different fibers may traverse the tract in in opposite directions forming a bidirectional connection, such as in parts of the spinal cord or in the corpus callosum. While diffusion anisotropy is not unique of the brain, as has been observed in crystals, muscles, and even fruits and vegetables. However, the degree of anisotropy in healthy white matter is greater than other tissues (Cleveland et al., 1976; Garrido et al., 1994; Henkelman et al., 1994). The overarching objective of current research on diffusion MRI is to answer if it is possible to directly map the diffusion measured parameters to specific microstructural components. Nonetheless, the complexity of the aforementioned structures; complex water transport trough membranes and ion-related cotransport mechanisms; variable inter-axonal space, diameter, myelin

thickness; and irregular, complex geometry with undulations deviating from an ideal cylinder are reasons why this question is unlikely to have a straightforward answer.

There is no direct relation between anisotropy observed and an specific microstructure characteristic. This is because axon density, packing, diameter, myelin thickness, and such, vary from tract to tract (Pierpaoli et al., 1996). Nevertheless, the degree of anisotropy is used as a biomarker of integrity of the white matter. Now, the questions are what components of the white matter influence this measure, and to what extent. Theoretically, the dense axonal cytoskeleton could impart a physical barrier to water diffusion perpendicular to axons, and generate magnetic susceptibility gradients affecting diffusivity measures. However, several studies in giant axons from animals (mainly marine life) have ruled out a role for neurofilaments and microtubules in the observed anisotropy in ordered axonal systems (Lian, Williams, and Lowe, 1994; Clark, Barker, and Tofts, 1999; Beaulieu and Allen, 1994a; Beaulieu and Allen, 1994b; Takahashi et al., 2002). Axonal Transport can affect directional diffusivity (Brangwynne et al., 2008), but the differential between $D_{\parallel}$ and $D_{\perp}$ remains constant. The remaining factors are the myelin coating of the axons, and the axonal membranes per se. Myelin sheaths in axons are not the only cause of anisotropic diffusion, as studies in newborn human and rat babies, *in vitro* unmyelinated nerves, and mutant demyelination animal models, have shown anisotropy can be measured even before myelin is deposited, or not deposited at all (Wimberger et al., 1995; Aung, Mar, and Benzinger, 2013; Bar-Shir, Duncan, and Cohen, 2009; Kasprian et al., 2008; Liu et al., 2011). These are important results, as they mean diffusion anisotropy cannot be used as a quantitative marker of myelin content. Myelin has a supporting role on diffusion anisotropy, and modulates the degree of anisotropy. While myelin does correlate with reduced perpendicular diffusion, so does axon packing, so distinguishing which of the two factors contributed to the measured change is difficult. It is then the axonal membrane the main contributor to the degree of anisotropy, while myelin has a secondary role.

There have been multiple studies which detected correlation with diffusivity and microstructural features; such as anisotropy, mean diffusivity, parallel and orthogonal changes, with axon count and density, and myelin count and density, in multiple sclerosis patients *post mortem* (Mottershead et al., 2003; Klaus Schmierer et al., 2008; Seewann et al., 2009; Klawiter et al., 2011; Kolasinski et al., 2012; Moll et al., 2011); anisotropy with myelin in the development of fetuses (Saksena et al., 2008); axonal density in Alzheimer patients *post mortem* (Gouw et al., 2008); various changes in diffusivity with free radical injury in elderly (Back et al., 2011); and axonal membrane circumference and others in patients with temporal lobe epilepsy (Concha et al., 2010).

2.3.3 Compartments

Another factor affecting the diffusion is the compartmentalization of the white matter and crossing fibers. The axonal membrane has a finite permeability, and hinders the water movement across it. As discussed earlier in the first section, and will be expanded later on Chapter 3, the signal measured corresponds to a sample of the Ensemble Average Propagator (EAP), so the propagator of the intra-axonal and intra-cellular compartments is mixed and averaged with the one of the extra-axonal space. Thus, it could be a problem if, for example, an anomaly in tissue generates an increment of diffusion in a intra-axonal compartment, and an decrement of the same magnitude in the extra-axonal

compartment. This would effectively results in an unchanged net diffusion measured, even if there has been a change in the microstructure. One should take into account this structural segregation of water to model diffusion precisely.

2.3.4 Side note: anomalous diffusion

For all this to work, the main condition is to assume there is no strange conditions that affect the diffusion in ways that the Brownian motion model stops working. However, there are very specific cases where the coarse grained diffusion coefficient does not converge to a positive value. There are two cases, when $D_{\Delta\to\infty} = 0$ (subdiffusive behavior), and when $D_{\Delta\to\infty} = \infty$ (superdiffusive behavior). This means that anomalous diffusion means the macroscopic diffusion coefficient does not exist. This can happen in inhomogeneous media, where it can be modelled as quenched disorder in local hopping rates (Bouchaud and Georges, 1990). One trivial case is where there are compartments that completely confine water movement, where this is considered subdiffusive behavior. Anomalous diffusion can occur when there is a fractal like structure, which means the statistics of the structural fluctuations are similar at different scales. Thus, the substrate never looks homogeneous, even when increasing the graining scale. Another cause is the existence of a macroscopic active random flow (Kravtsov, Lerner, and Yudson, 1985). Anomalous diffusion do not seem to exist in the brain (Mussel, Inzelberg, and Nevo, 2017; Novikov, Fieremans, et al., 2019).

Chapter 3

MRI And Its Quirks

Nuclear Magnetic Resonance Imaging is a very powerful tool in medical diagnosis and research. Is a non invasive imaging technique that exploits the atomic magnetic structure of an object to obtain the image of various properties from inside the object, without the necessity to dissect it.

3.1 MRI In A Nutshell

Water molecules are made of two atoms of hydrogen and one of oxygen. In its more abundant isotope, hydrogen atom nuclei are solely constituted of one proton. Letting quantum effects aside, one can say the spinning nucleus with an electrical charge (commonly called spin) will induce a small magnetic field, and the particle will become a magnetic dipole. When a uniform and strong magnetic field is applied to a subject, two important phenomena will happen. The first is that the spins will align to the direction of the field, some aligning directly, and some pointing opposite, depending on their energy state (one low and one high). The second is that the spins will not simply align toward or against the field, but actually precess along that direction. More importantly, the frequency ω_P of precession is proportional to the local magnetic field strength B_l, described by the Larmor equation,

$$\omega_P = \gamma B_l. \tag{3.1}$$

An MRI machine is capable of modulating the local strength of the magnetic field through the subject, by using a powerful permanent superconducting magnet and coils inducing homogeneous gradients. This changes the precessing frequency of the spins and its phase in a predictable way. The machine also has an antenna capable of transmitting and receiving radio frequency pulses. If a pulse of an arbitrary frequency is emitted in the vicinity of a set of spins precessing at the same frequency, the spins will resonate and become excited by absorbing the energy of the pulse. This excitation causes the flipping of more spins to align to the direction of the higher energy state, and will align their precession phase. In a normal state, all spins point to random directions and precess in different frequencies. Thus, the magnetic moment of the dipoles will mainly cancel each other. In the other hand, if the spins are precessing at the same frequency and in-phase, their contributions will add up to a net rotating magnetization vector. This magnetization can be measured by the same antenna. The speed of relaxation (the dissipation of the energy absorbed from the radiofrequency pulse) will depend on the properties and microestructure of the tissue being excited. Furthermore, the exact location where the

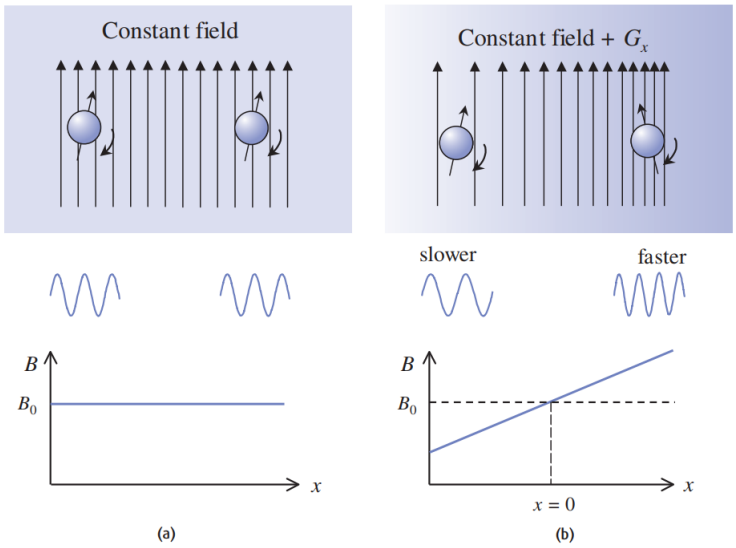

FIGURE 3.1: Effect of field gradient on nuclei. (a) B_0 (permanent magnet field) only, all nuclei precess at the same frequency. (b) B_0 plus homogeneous gradient G_x. Precession frequency now depends upon position. Adapted from McRobbie et al., 2017.

signal is being generated can be inferred by using the gradient coils. The directional magnetic gradients will slightly change the phase and frequency of precession depending on the position of the tissue (Figure 3.1). Finally, the position of the signal can be recovered by transforming back from the frequency space to the spatial space.

This is a very superficial explanation of the process. For a more in-depth explanation please refer to Grover et al., 2015 and Klioze, 2013.

3.2 Diffusion Weighted Imaging

As discussed in Chapter 2, the diffusion propagator describes the probability of displacement of spins, and is dependent of the chosen diffusion length. The propagator form is the result of autodiffusion hindered by white matter microstructure. It is then evident that one should be able to obtain information of the brain microstructure by computing this propagator. Diffusion Weighted Imaging (DWI) works indirectly sampling the diffusion propagator. This is done by means of MRI and cleverly crafted magnetic pulse sequences to measure the displacement of the set of diffusing spins being observed.

3.2.1 The Bloch-Torrey equation

Remember that the magnetization vector is the property the MRI machine is capable of measuring. In the stricter sense, the machine is only capable of measuring the projection of this vector in the plane orthogonal to the main static field $\boldsymbol{B}_0$. This is called the transverse magnetization, while the component parallel to the field is called the longitudinal magnetization.

The Bloch-Torrey equations model the change of the magnetization of a continuum of spins in a strong magnetic field, considering the effects of diffusion movement,

$$\frac{\partial \boldsymbol{M}}{\partial t} = \gamma \boldsymbol{M} \times \boldsymbol{B}_0 - \frac{M_x \boldsymbol{e}_i + M_y \boldsymbol{e}_j}{T_2} - \frac{M_z - M_0}{T_1}\boldsymbol{e}_k - \nabla \cdot (\boldsymbol{D} \nabla \boldsymbol{M}), \tag{3.2}$$

where $\boldsymbol{e}_i, \boldsymbol{e}_j, \boldsymbol{e}_k$ are the canonical basis of the 3-dimensional Cartesian space, $\boldsymbol{M}$ is the magnetization vector of the continuum, γ is the gyromagnetic constant of the medium, T_1, T_2 are the relaxation times of transversal and longitudinal magnetization, and M_0 is the steady state magnetization of the system as $t \to \infty$ (Torrey, 1956) (Hall, 2016). A common simplification only takes into account the transverse magnetization, represented as a 2-dimensional vector, which in turn is represented as a complex number (Bloembergen, Purcell, and Pound, 1948) (Abragam, 1961).

$$\frac{\partial m(t, \boldsymbol{r})}{\partial t} = \nabla_{\boldsymbol{r}'} \cdot [\boldsymbol{D}(\boldsymbol{r}') \nabla_{\boldsymbol{r}'} m(t, \boldsymbol{r})] - [T_2^{-1}(\boldsymbol{r}) + i\omega_O(t, \boldsymbol{r})] m(t, \boldsymbol{r}). \tag{3.3}$$

Here, $\omega_O = \omega(\boldsymbol{r}) + \boldsymbol{G}(t)\boldsymbol{r}$ is the Larmor Frequency offset. The term $\boldsymbol{G}(t)\boldsymbol{r}$ comes from the diffusion sensitizing magnetic gradients generated by the machine, and $\omega(\boldsymbol{r})$ comes from the intrinsic magnetic microstructure of the underlying tissue.

3.2.2 *qt* Imaging

The fundamental link between the diffusion propagator in (2.4) and the MRI signal lays in the gradient-dependent phase. The main technique used to exploit this is the Pulsed Gradient Spin Echo (PGSE) sequence. The PGSE was first demonstrated by Stejskal and Tanner, 1965; based on the ideas of McCall, Douglass, and Anderson, 1963. It consists in a sequence of radio frequency pulses of 90° an 180°, and spatially homogeneous gradient pulses of different directions to dephase diffusing spins, and attenuate the resulting signal as a result of this dephasement. A more thorough explanation can be found in Rios-Carrillo, 2017 (in Spanish). An important detail is the definition of the $\boldsymbol{q}$ vector, which condenses various experimental parameters of the MRI sequence. Also known as the wavevector, $\boldsymbol{q}$ is defined as

$$\boldsymbol{q} = \gamma \delta \boldsymbol{G}. \tag{3.4}$$

Here, γ is the gyromagnetic ratio, δ is the gradient pulse duration. Here we drop the time dependence of gradient $\boldsymbol{G}$.

Stejskal and Tanner described the analytic expression of the MRI signal attenuation in the PGSE experiment when very narrow rectangular gradient are used, so $\delta \to 0$. This is called the *narrow gradient approximation*. While the approximation is impossible to realize in a real machine, it brings very important insights on the behavior of the signal when $\delta << \Delta$. Let $S(t, \boldsymbol{q})$ be the signal acquired using the sequence parameters represented by $\boldsymbol{q}$ along diffusion time t, and V the voxel being measured. $S(\Delta, \boldsymbol{0})$ is the signal not weighted to diffusion along time Δ, so the effect of T_2 relaxation is removed from the normalized signal. Being the MRI signal the net magnetization $\int m(t, \boldsymbol{r}) d\boldsymbol{r}$, the normalized signal attenuation under these conditions is

$$\frac{S(\Delta, \boldsymbol{q})}{S(\Delta, \boldsymbol{0})} = \int_V P(\boldsymbol{r}_0) \int P(\boldsymbol{r}_0 | \boldsymbol{r}', \Delta) \exp(-i\boldsymbol{q}^T [\boldsymbol{r}' - \boldsymbol{r}_0]) d\boldsymbol{r}' d\boldsymbol{r}_0. \tag{3.5}$$

The dephasement terms are only dependent on the displacement vectors, and (3.5) can be transformed similarly as in (2.4),

$$\frac{S(\Delta, \boldsymbol{q})}{S(\Delta, \boldsymbol{0})} = \int G_{\bar{\boldsymbol{r}},\Delta} \exp(-i\boldsymbol{q}^T\bar{\boldsymbol{r}}) d\bar{\boldsymbol{r}}, \tag{3.6}$$

where

$$G_{\bar{\boldsymbol{r}},\Delta} = \int_V P(\boldsymbol{r}_0) P(\boldsymbol{r}_0|\boldsymbol{r}_0 + \bar{\boldsymbol{r}}, \Delta) d\boldsymbol{r}_0. \tag{3.7}$$

Doing this, we discover that the signal in (3.6) is the Fourier transform of $G_{\bar{\boldsymbol{r}},\Delta}$ at $\boldsymbol{q}$. Also important, (3.7) is the averaging, as in (2.6), of the local ensemble propagators $\langle P(\boldsymbol{r}_0|\boldsymbol{r}_0 + \bar{\boldsymbol{r}}, \Delta)\rangle_{\boldsymbol{r}_0}$ over all starting positions. This is called the *Ensemble Average Propagator*, or EAP (Kärger and Heink, 1983). One should note the EAP is invariant to the starting point, and quantifies the probability that a spin displaced $\bar{\boldsymbol{r}}$ from their starting point after a time Δ.

In summary, the parameters of the Diffusion MRI consists in the diffusion time Δ and the vector $\boldsymbol{q}$.

3.3 Diffusion Tensor Imaging

We mentioned earlier the effects of diffusion time in the scale of the information of microstructure that can be extrapolated from the retrieved signal. In this work, we focus on the coarse regime, when the difussion time is long enough to average out the fine-grain details of the microstructure, and simplify the model to near-gaussian difussion. When the difussion length L is considerably greater than any of the distances of the microscopic features, the parameter space of the measures can be simplified.

3.3.1 Enter the b-value

The b-value (Le Bihan, Breton, et al., 1986) is a condensation of the parameters in qt imaging when the diffusion in every compartment in the voxel is Gaussian. This can happen if the substrate is guaranteed to have a Gaussian diffusion profile, or if one attains the coarse graining regime with a long enough diffusion time. The white matter is a very complex substrate with rich details, with highly non Gaussian diffusion. This means the second approach needs to be used.

$$b = \boldsymbol{q}^T\boldsymbol{q}\Delta. \tag{3.8}$$

The actual form of the diffusion time here is $\Delta - \delta/3$ instead of just Δ, however, we neglect δ on the assumption that $\delta << \Delta$.

3.3.2 Signal from Gaussian diffusion.

The form of the Ensemble Average propagator when diffusion is Gaussian was discussed on Chapter 2. If we substitute the multivariate Gaussian distribution form of (2.4) in the signal expression, we obtain the tensor model.

$$\frac{S(\Delta, \boldsymbol{q})}{S(\Delta, \boldsymbol{0})} = \frac{S(b, \boldsymbol{g})}{S_0} = \exp(-b\boldsymbol{g}^T\boldsymbol{D}\boldsymbol{g}). \tag{3.9}$$

This is the fundamental model of Diffusion Tensor Imaging. Now on, we refer the unweighted signal $S(\Delta, \boldsymbol{0})$ as S_0 for convenience. We can normalize the gradient direction $\boldsymbol{g}$, as the magnitude information is already in b.

3.3.3 Multiple compartments and crossing fibers

The most important limitation of DTI is that is unable to describe diffusion on substrates with multiple compartments, in which water is restricted to travel between them (Panagiotaki et al., 2012). As was discussed on the anatomy section of Chapter 2, this is the case of the diffusion on white matter. Each compartment has a Gaussian diffusion profile in the coarse graining regime. The multitensor model overcomes some of the limitations by modeling the EAP of a voxel with compartments as a mixture of Gaussian densities,

$$G^{voxel}_{\bar{\boldsymbol{r}},\Delta} = \sum_i^n f_i \mathcal{G}_{\bar{\boldsymbol{r}}}(\boldsymbol{D}_i, \Delta), \tag{3.10}$$

where $\mathcal{G}$ is a multivariate Gaussian density with mean $\boldsymbol{\mu} = \boldsymbol{0}$ and covariance matrix $\boldsymbol{\Sigma} = 2\Delta\boldsymbol{D}$ evaluated at $\bar{\boldsymbol{r}}$. The model consists in n bundles of fibers, each one using a part of the volume of the whole voxel. There is no water exchange between different bundles. The fraction of the volume used by each bundle is denoted by $0 < f_i < 1$. Each value of f is the volume fraction of the compartment. In the context of brain MRI, this is called Intra Cellular Volume Fraction, Intra Axonal Volume Fraction, or just Volume Fraction depending if the compartment is a neuronal axon, or water inside glia or other cells. The sum of all weights of each compartment must add to 1, including hindered diffusion outside any compartment. Thus, the normalized signal has form

$$\frac{S(b, \boldsymbol{g})}{S_0} = \sum_i^n f_i \exp(-b\boldsymbol{g}^T \boldsymbol{D}_i \boldsymbol{g}). \tag{3.11}$$

One problem of the multitensor model is the high count of degrees of freedom. Each fiber bundle has its own diffusion tensor and volume fraction, meaning $7n - 1$ parameters. This might cause instability. However, one can restrict the number of parameters by assuming constraints like radial symmetry and negligible orthogonal diffusion. In this work, we use models with these characteristics, as will be discussed on Chapter 4.

The number of compartments n is assumed to be known. Practical handicaps, which will be discussed on the next section, limit the number of orientations the method can resolve reliably and most applications consider a maximum of 2 (Alexander and Seunarine, 2010).

3.4 Diffusion MRI outside the blackboard

The MRI Diffusion weighted image analysis is not only limited by their intrinsic sampling method. The models formerly described do not take all the real world intricacies of the measuring process. There are a variety of phenomena that obfuscate scanning the medium. MRI has several such as Rician-distributed background noise (Edelstein, Bottomley, and Pfeifer, 1984) (Basser and Pajevic, 2000), magnetic disturbances caused by tissue susceptibility or air-tissue interfaces, frequency and sampling related artifacts.

In addition to all of this, there are problems particular to Diffusion Weighted Imaging (Le Bihan, Poupon, et al., 2006), which are listed below.

- Limitations of the dephasing gradients. The electronics and coils needed to generate the strong gradients needed are physically limited. Gradient pulses are not perfectly sharp, and they have limited intensity. This is sometimes compensated by using longer gradient pulses. However, this deviates from the small-δ assumption, and makes the signal more difficult to treat and interpret.
- Eddy currents induced by the switching magnetic fields. The alternating magnetic field induces electric currents in conductive surfaces of the MRI scanner machine, which in turn create magnetic which contaminate the main field and gradients. These artifacts could lead to dilation and shear of the image. The b-value induced to the spins differs from the expected value, leading to over- or underestimation of the diffusivity. This is an important issue, as the b-value is related to the gradient magnitude squared.
- Motion artifacts related to *in vivo* measures. A human or animal subject cannot stay perfectly static. The dephasing induced by macroscopic movement is up to 100 time larger than those induced by diffusion. These will induce ghosting, typically in the phase-encoded direction of MRI. Breathing an blood circulation. This can lead to the overestimation of the Apparent Diffusion Coefficient. Some ways of controlling this are gated acquisitions with EKG or breathing signals, navigator echoes and sedation.
- Echo Planar Imaging (EPI) artifacts. EPI is widely used for DW-MRI because it practically solves the movement artifacts. An EPI image takes 100ms to be taken. However, EPI has limited spatial resolution, which in turn generates ghosting. Also, T_2 decaying is a concern.
- The real diffusion time is not known. The theory in PGSE says the diffusion time should be $\Delta - \delta/3$, however, its physical significance is not so clear. as diffusion effects during gradient pulses and in between do not scale the same way with time (Jones, 2010). Lori, Conturo, and Le Bihan, 2003 say $\Delta + \delta$ is a better option. If δ is neglected, underestimation of diffusivity might occur (Mitra and Halperin, 1995).
- The choice of b is a tradeoff between high signal at low b and more detailed angular structure at high b (Basser, 2002).

3.5 Modeling Diffusion inside White Matter

Imagine a car for a moment, and the individual parts that make it. There is a very complex engine which converts chemical energy to mechanical energy by means of combustion or electromagnetism, a transmission which converts the torque of the motor, wheels specially designed to optimize traction, a chassis designed to protect the passengers in an accident, a plethora of electronics controlling everything, etc. Notwithstanding such degree of complexity, one does not need to have advanced degrees in mechanical and electrical engineering to drive a car. Even if one person completely ignores the underlying mechanisms that make the car move, it is absolutely possible for this person to

drive it, *given that such person knows the relevant dynamics and parts of the system*. In this example, the important variables would be the switch, brake, accelerator, clutch (if there is one), steering wheel and gear stick. The dynamics are the mental representations of the start sequence, how the car steering would respond at a given speed, the braking process, and such. This, of course, does not imply the driver knows the whole physics of the moving car, but just an *effective* abstraction of it.

An effective theory proposes to describe a certain set of observations without explicitly implicating that the mechanism employed in the theory corresponds directly to the actual causes of the observed phenomena the theory is being fitted to. As discussed in Chapter 2, coarse graining is very important in Diffusion MRI. The quantum mechanics of the nanometre scale are averaged out and become negligible for most of the imaging techniques. In the same way, microscopic jittering of the water molecules on the micrometre scale acquires a Gaussian diffusion profile at the coarse grained regime on the millimetre scale. At this scale, only some of the plethora of physical degrees of freedom characterizing diffusivity remain relevant (Novikov and Kiselev, 2010). This coarse graining in MRI arises very naturally, as diffusion by itself is a coarse graining of the Brownian movement in the form of the mean squared displacement and the EAP.

3.5.1 Model versus Representation

The mere concept of what is a model still is debated, and varies between discipline. One of such interpretations defines the model as a particular case of a physical theory, an instance of this theory with only conserves relevant degrees of freedom, and normally is expressed in terms that make comparison with real life measures of the modelled phenomena easy (Novikov, Kiselev, and Jespersen, 2018). Ergo, a crucial point is that a model is derived from a *sketch* of reality, a pictorial representation of the phenomena. Depending on the scale of averaging used, there may be different models which predict measurements on that resolution in particular. Nonetheless, all those models are unified under a common theory. When a mathematical expression merely fits the observations well, but lacks this theoretical framework, it becomes a *representation*.

In a theory of axons as cylinders of finite radius, one can use strong gradients and short diffusion times to capture this microstructure information. However, another model is better suited to the coarse grained regime. When diffusion length is significantly greater than the axon radii, the effective theory becomes that of zero radius channels, or *sticks*. This means axonal diameter becomes an irrelevant parameter when using long temporal scales and low diffusion weighting.

The division between model and representation can be subtle, and it is important to know what is being used in any given situation. Novikov, Kiselev, and Jespersen, 2018 provide an interesting example about bi-exponential fitting as a two compartment model, and that justifying the model assumptions is much less trivial and more impactful than doing the fitting *per se*.

3.5.2 DTI beyond Gaussianity

By establishing this semantic delimitation, it happens to be that DTI is not a model *per se*, but a signal representation. DTI can be seen as a special case of the so-called cumulant expansion, which is a Taylor expansion of the diffusion signal around $\boldsymbol{q} = 0$ (Kiselev,

2010). DTI makes no assumptions on the underlying tissue microstructure. Contrary to what is still often stated in the literature, DTI is not based on the Gaussian diffusion assumption either. Rather, it captures only the lowest-order term in the cumulant expansion. Any reasonable biophysical model of diffusion has a DTI representation to which it reduces in the limit of $b \to 0$. However, this same logic classifies DTI as a model of the absence of any microstructure at the micrometer scale. It is not the anisotropy, but the absence of higher-order terms in the cumulant expansion that constitutes a model of this. Recognizing DTI as a representation at low diffusion weighting rationalizes its widespread clinical applicability in the face of unfair criticism, given that diffusion is almost always non Gaussian in the brain.

Chapter 4

Methodology

4.1 Synthesis of Spin Trajectories

The measurement process in a MRI machine introduces noise and artifacts. To find the theoretical limit that can be inferred from these signals, one would need to be able to measure the physical process directly. This implies knowing the exact position of each magnetic dipole, currently an intractable task. A more practical approach is the use of simulation. Each spin trajectory is the product of collisions and thermal energy. Trying to model and simulate these interactions for a realistically large number of spins would be computationally intractable, as the number of spins in White Matter is roughly 2.4×10^{10} per μm^3 (Filo and Mezer, 2018). Fortunately, one can rely on the probabilistic formulation of the problem. The phenomenon can be approximated by simulating the random behavior of a relatively large ensemble of particles; a Montecarlo simulation of the diffusive process. In that way, we are sampling the process with a reasonable degree of accuracy.

The simulation of the spin dynamics works by displacing each of the molecules at equidistant discrete time steps, and computes the elastic collision between them and the substrate. The displacement has a random direction and a fixed step length. The step length is calculated as a function of the diffusion coefficient of the medium and the duration of each time step. For an in-depth explanation of the simulation algorithm used and convergence constraints refer to Hall and Alexander, 2009.

Along with exactly determining the trajectory of the particles, another benefit is the quality of the obtained signal. The synthetic signal is completely free of noise and common measurement artifacts, such as movement of the subject and eddy currents. Ergo, we are capable of obtaining just the modeling error by factoring out every other source of variability without further post processing. Consequently, we can establish a lower bound of the expected error using this technique.

We synthesized the walks of large set of simulated particles using CAMINO Montecarlo diffusion simulator (Cook et al., 2006). We simulated water diffusion on idealized substrates based in histology, which resembles some characteristics of real white matter (Figure 4.1). The substrate is formed by a set of parallel, non abutting cylinders (simplified axon model) randomly packed, whose diameter has a gamma distribution derived from electron microscopy of the corpus callosum (Aboitiz et al., 1992) (Assaf et al., 2008).

4.1.1 Rotated Bundles

CAMINO is capable of simulating a crossing between two fiber bundles. However, the software has two main drawbacks. Their crossing fiber implementation is limited to lesser complexity substrates; parallel cylinders equidistantly packed, and of equal diameter. Also, the spins position cannot be initialized separately to guarantee the same number of spins in both compartments. This restriction is important because the quality of the signal is dependent of the number of spins, so we need to use the same number for both of the compartments to attain comparable quality. A solution we implemented in this thesis work to tackle these problems is to take the same spin walks in complex substrates we already have, and then rotate the ensemble trajectory for all the simulation history. Then, it is possible to add the signals of both of the bundles to simulate the signal of a crossing. It is still disputable whether fibers interdigitate at axon or bundle level. Nevertheless, literature generally assume crossings of separated whole bundles, and models of such fashion have corresponded with known fiber anatomy (Tuch et al., 2002). We assumed bundle level interdigitation to simplify the signal generation, and to allow the use of the somewhat realistic substrate used.

4.1.2 Simulation Parameters

TABLE 4.1: Parameters used in simulation.

Parameter		Value
N	Number of spins	500,000
T	Number of time steps	4,000
t_{sim}	Duration of the simulation	0.0359 s
D_{sim}	Diffusion coefficient of the medium	2.1×10^{-9}
l_{voxel}	Cubic voxel side length	35 µm
	Random Seed	60,476,047

The simulation parameters, such as number of molecules and time steps were chosen to have good convergence of the simulation (see table 4.1). The voxel size and substrate need to be taken into account. For our main dataset, we choose D_{sim}; the free diffusion coefficient of the medium, as the estimated intra-axonal infinite time diffusion coefficient measured *in vivo* inside the brain (Dhital et al., 2019). The number of cylinders is chosen to generate six substrates of different intra-axonal volume fraction f (also called Intra Cellular Volume Fraction or ICVF) separated approximately by increments of 0.1 (see table 4.2). The substrate is periodic in the simulation, so if a spin exits the voxel, it will find another identical substrate layout.

The spins initial position was randomly distributed along the substrate in an uniform fashion. Two positions sets are generated with the same number of spins. One set is initialized just inside the axons (the intracellular or intra axonal space), the other set, outside the axons (also called the extracellular or extra axonal space). Both sets are simulated separately. In this way, we guarantee the signal of both of the the two compartments has the same quality and same S_0 weighting.

TABLE 4.2: Intra-axonal Volume Fraction levels with its respective labels and number of cylinders used.

Level	N_{cyl}	f
lvl2	170	0.2028451907672634
lvl3	260	0.3081223234273966
lvl4	330	0.4014456195874796
lvl5	412	0.5016271405754553
lvl6	490	0.6076080511924874
lvl7	580	0.7064550523980454

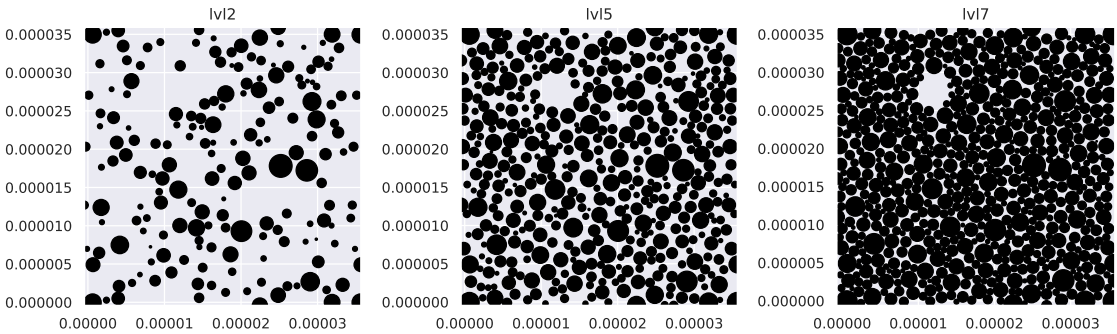

FIGURE 4.1: Transversal cut of low, medium and high f substrates. This synthetic substrate tries to imitate the axon distribution of real white matter, like in Figure 1.1.

4.1.3 MRI Signal Measurement

We use the CAMINO toolkit to compute MRI signals from the synthesized spin trajectories. We simulate Stejskal-Tanner standard PGSE sequences (Stejskal and Tanner, 1965) in order to be able to perform experiments on the signal space of the simulations. Two protocols are used. One has 4 shells (b-values), each one with 90 directions (see figure 4.2 and appendix A). The other is a subset of the former which contains only the first shell $b = 1000$ with 90 directions. These protocols are crafted with parameters to reduce δ to a very small value (See table 4.3). We chose Δ long enough to achieve the coarse grain regime discussed on Chapter 2 (assuming it is equal to the diffusion time, given that the small δ approximation holds). It has been shown this is a reasonably long time for substrates of similar size (Burcaw, Fieremans, and Novikov, 2015).

TABLE 4.3: Parameters of used pulse sequence.

Parameter		Value
b	b-value	$\{1000, 1500, 2000, 2500\} \times 10^6$
$\|G\|$	Gradient magnitude	$\{1.259, 1.543, 1.781, 1.991\}$
Δ	Delay between gradient pulses	0.0354
δ	Duration of the gradient pulses	0.0005
TE	Echo Time	0.0359

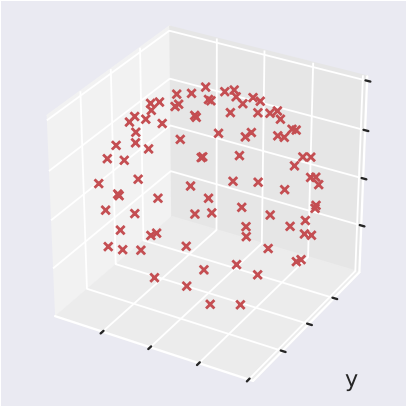

FIGURE 4.2: Directions in PGSE scheme used.

4.1.4 Displacement Set and Ground Truth Computation

For each of the simulations, the set of displacement vectors is computed by subtracting the final position of each spin from its initial. Let $\boldsymbol{r}_i|_t$ be the position of the i-th spin at time t. Thus, we define

$$\overline{\boldsymbol{P}} = \{\overline{\boldsymbol{r}_i} \in \mathbb{R}^3 : \overline{\boldsymbol{r}_i} = \boldsymbol{r}_i|_{t_{sim}} - \boldsymbol{r}_i|_0\}. \tag{4.1}$$

Then, we compute the Mean Squared Displacement of the set by averaging all the displacement vectors squared elementwise.

$$\langle \overline{\boldsymbol{r}}^2 \rangle = \frac{1}{N} \sum_{\boldsymbol{r}_i \in \overline{\boldsymbol{P}}} \overline{\boldsymbol{r}_i}^2. \tag{4.2}$$

The apparent diffusion coefficients along the axis can be computed using (2.7). We define the ground truth apparent parallel diffusion coefficient $D_{\parallel}$ as the diffusion along the y axis. We assume the orthogonal diffusion is equal in any direction perpendicular to z, so we average the diffusion along x and y to obtain the orthogonal ground truth $D_{\perp}$. The ground truths are computed as

$$D_{\parallel} = \frac{\langle \overline{\boldsymbol{r}}^2 \rangle_z}{2t_{sim}} \tag{4.3}$$

and

$$D_{\perp} = \frac{1}{2} \frac{\langle \overline{\boldsymbol{r}}^2 \rangle_x + \langle \overline{\boldsymbol{r}}^2 \rangle_y}{2t_{sim}}.$$

However, the diffusion time we are measuring with the MRI diffusion protocol is not the whole time of the simulation, but the effective time Δ. To account for the difference in the calculation of the ground truths, we model the effect of the active pulsed gradients on a spin as an averaging of the walking along all the time the gradient is on. To do this, we generate a new pseudo displacement vector set by taking the beginning and end of the displacement of each spin as the centroid of its location history for $0 \leq t \leq \delta$ and

$(t_{sim} - \delta) \leq t \leq t_{sim}$ respectively.

$$\overline{\boldsymbol{P}_\delta} = \{\overline{\boldsymbol{\mu}_i} \in \mathbb{R}^3 : \overline{\boldsymbol{\mu}_i} = \boldsymbol{\mu}_i|_{0,\delta} - \boldsymbol{\mu}_i|_{(t_{sim}-\delta),t_{sim}}\}, \tag{4.4}$$

where $\boldsymbol{\mu}_i|_{a,b}$ is the average of all the position history of the i-th spin from time a to b. We use (4.3) to recompute the ground truths, but now using time Δ instead of t_{sim}. They are very similar (less than 2% difference) to the ones obtained originally, meaning the estimation works well because of our assumption that $\Delta << \delta$.

Finally the complete bundle diffusion coefficients are computed as the weighing of the intra-axonal and extra-axonal compartments by the ICVF.

$$\begin{aligned} D_{\perp,bundle} &= fD_{\perp,intra} + (1-f)D_{\perp,extra} \\ D_{\parallel,bundle} &= fD_{\parallel,intra} + (1-f)D_{\parallel,extra}. \end{aligned} \tag{4.5}$$

TABLE 4.4: Ground truth values of the synthetic dataset. Computed from the pseudo displacement set with $\delta = 0.0005$.

Compartment	$D_\perp$		$D_\parallel$	
f	extra	intra	extra	intra
lvl2	1.676e-09	3.094e-12	2.093e-09	2.085e-09
lvl3	1.481e-09	2.647e-12	2.085e-09	2.096e-09
lvl4	1.335e-09	2.606e-12	2.098e-09	2.092e-09
lvl5	1.162e-09	2.464e-12	2.089e-09	2.094e-09
lvl6	9.930e-10	2.559e-12	2.089e-09	2.090e-09
lvl7	7.948e-10	2.433e-12	2.092e-09	2.095e-09

4.2 Tensor Fitting to MRI Simulated Signal

Histograms are a conceptually interesting approach to observe the structure of the diffusion movement. However, the main task is to assess this structure using the data from an MRI machine; a limited set of samples from indirect measurement of the phenomenon.

A diffusion tensor is fitted by finding the set of parameters $\boldsymbol{p}$ which minimize the difference between the simulation signal vector $\boldsymbol{S}_{sim}$, and the ideal signal generated by a model of the process,

$$\underset{\boldsymbol{p}}{\operatorname{argmin}} \left\| \boldsymbol{S}_{sim} - \boldsymbol{S}_{model}(\boldsymbol{p}) \right\|_1, \tag{4.6}$$

where $\|\boldsymbol{v}\|_1 = \sum_i |v_i|$ is the Taxicab or L_1 norm of vector $\boldsymbol{v}$.

4.2.1 Zeppelin Model

The main idea in DTI is to assume the shape of the propagator is entirely Gaussian. The first model comes from the solution of the Bloch-Torrey equation in a PGSE experiment

in heterogeneous gaussian diffusion (Basser, Mattiello, and LeBihan, 1994).

$$S_{bundle,i} = S_0 \exp(-b_i \boldsymbol{g}_i^T \boldsymbol{D} \boldsymbol{g}_i), \tag{4.7}$$

where $\boldsymbol{D} \in \mathbb{R}^{3\times3}$ is the diffusion tensor, and $\boldsymbol{g}_i \in \mathbb{R}^3$ is an unitary vector; the i-th direction of the magnetic gradient specified in the MRI protocol. Each direction can have a different b_i depending on the MRI sequence. One special case is where the tensor has the same apparent orthogonal diffusion coefficients $D_\perp$ along x, y and one apparent parallel diffusion coefficient $D_\parallel$ along z. This model is known as the *zeppelin*, because the level plot of the quadratic form $g^T \boldsymbol{D} g$ forms an ellipsoid with radial symmetry (Alexander, 2008). The zeppelin is restricted so

$$\boldsymbol{D} = diag(D_\perp, D_\perp, D_\parallel). \tag{4.8}$$

In this case, the eigenvectors form an orthogonal basis parallel to the x, y, z axis. We denote $\boldsymbol{D}_{\theta,\phi}$ as the same diffusion tensor whose eigenvectors had been rotated in spherical coordinates angles θ, ϕ with the transformation $\boldsymbol{R}(\theta, \phi) \in \mathbb{R}^{3\times3}$. Because $\boldsymbol{D}$ is a real symmetric matrix, it can be decomposed as $\boldsymbol{\Phi\Lambda\Phi}^T$, where $\boldsymbol{\Phi}$ is an orthogonal matrix whose columns are the eigenvectors of $\boldsymbol{D}$, and $\boldsymbol{\Lambda}$ is a diagonal matrix with its eigenvalues. Thus, it follows that

$$\boldsymbol{D}_{\theta,\phi} = \boldsymbol{RDR}^T = \boldsymbol{R}(\boldsymbol{\Phi\Lambda\Phi}^T)\boldsymbol{R}^T = (\boldsymbol{R\Phi})\boldsymbol{\Lambda}(\boldsymbol{R\Phi})^T. \tag{4.9}$$

In this manner, we have a way of describing diffusion in terms of angles, the orthogonal and parallel coefficients. This model is useful in the case of a single unidirectional bundle of axons. However, it will not be able to describe the case in which there are a crossing of two or more bundles. The model can be easily generalized to take a crossing into account, by adding the contribution of the other bundle. This means weighting both of the signals by a mixing factor $0 \leq \alpha \leq 1$.

$$\boldsymbol{S}_m = \alpha \boldsymbol{S}_{bundle1} + (1 - \alpha)\boldsymbol{S}_{bundle2}. \tag{4.10}$$

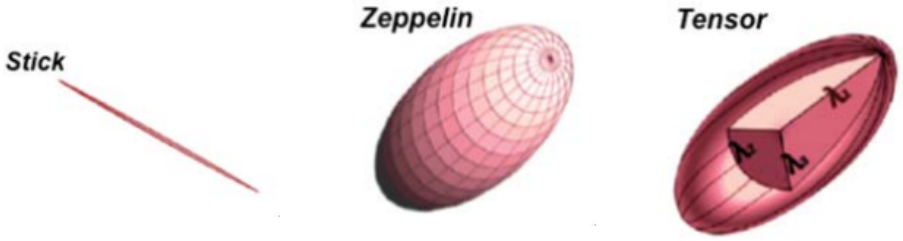

FIGURE 4.3: Graphical representation of the diffusion tensor and its special cases; the stick and zeppelin models. Adapted from Ferizi, Schneider, Panagiotaki, et al., 2014.

4.2.2 Stick + Zeppelin Model

The next logical generalization is to use two different compartments to model the propagator. In our substrate, radial diffusion inside the axons is highly restricted, because of impermeability and radii size. Therefore, it is reasonable to neglect the radial diffusion and assume the spins diffuse freely along the $\boldsymbol{d}_\theta$ axis parallel to the cylinders. Thus, we can assume a degenerated case of (4.7) with $D_\perp = 0$,

$$S_{intra,i} = S_0 \exp(-b_i D_\parallel (\boldsymbol{g}_i^T \boldsymbol{d}_{\theta,\phi})^2), \tag{4.11}$$

where $\boldsymbol{d}_{\theta,\phi}$ is the canonical vector $\boldsymbol{e}_z$ (an unit vector parallel to the z axis) with the rotation $\boldsymbol{R}_{\theta,\phi}$ applied. This part of the model is called the *stick*, because the level plot of the function would be just a line in a 3D space (Behrens et al., 2003). The extracellular space is fitted with the same approach as the *zeppelin* model,

$$S_{extra,i} = S_0 \exp(-b_i \boldsymbol{g}_i^T \boldsymbol{D}_{\theta,\phi} \boldsymbol{g}_i). \tag{4.12}$$

To form the complete signal of a bundle, the signals are added, weighted by the intra-axonal fraction f.

$$\boldsymbol{S}_{bundle} = f\boldsymbol{S}_{intra} + (1-f)\boldsymbol{S}_{extra}. \tag{4.13}$$

In the case of one crossing, two bundles are added weighted by the mix factor α, exactly like in (4.10).

4.3 Local Grid Search

Formulations (4.23) - (4.24) and (4.6) are nonlinear optimization problems that can be solved in a variety of ways. However, we are interested in isolating the error of the model, so we want to characterize the search space near the correct solution.

We solve previously stated optimization problems by searching in a grid of the discretized parameters. Each discretization has two parameters. The first one is the size of the neighborhood ϵ, that represent a percentage of the ground truth value p. As an example, a value of $\epsilon = 0.999$ means that the partition spans $\pm 99.9\%$ of the nominal ground truth value (i.e from $(0.001)p$ to $(1.999)p$). The second parameter is the number of points N_{grid} in the partition. We have $N_{grid}+1$ equidistant points from $(1-\epsilon)p$ to $(1+\epsilon)p$.

$$\boldsymbol{\Omega}_p = \{P_i = i\frac{2\epsilon p}{N_{grid}} + (1-\epsilon)p \ , \ i \in \{0,1,\cdots,N_{grid}\}\}. \tag{4.14}$$

The complete search space $\boldsymbol{\Omega}$ is an n-dimensional grid result of the Cartesian product of all parameter discretizations for each of the free parameters depending of the search. Supposing we are using n parameters, all with the same N_{grid}, the search space looks like this:

$$\boldsymbol{\Omega} = \boldsymbol{\Omega}_{p_1} \times \boldsymbol{\Omega}_{p_2} \times \cdots \times \boldsymbol{\Omega}_{p_n} \ , \ \boldsymbol{\Omega} \in (\mathbb{R}^{N_{grid}+1})^n. \tag{4.15}$$

An exhaustive search is done, and we select the point in this grid (i.e. the combination of parameters) that has the minimum norm.

4.4 Overview of Experiments and their Degrees Of Freedom

Leaving details of microstructure aside, one can parametrize a pair of fiber bundles crossing by their respective pair of diffusion coefficients, their pair of angles in spherical coordinates, the ICVF f, and the mixing factor α. Using our methodology on all of these parameters is computationally intractable, for a meaningful resolution. The Grid Search complexity grows $O(N_{grid}^{\#p})$, so we simplify the search in a number of ways:

- One of the bundles is always parallel to the z axis.
- The other bundle rotates just around the y axis in the xz plane. We call this rotation angle θ, and is measured starting from the z axis.
- Both of the bundles share the same simulation parameters, so they will have the same f, $D_{\parallel}$ and $D_{\perp}$.
- The mixing factor α is always 0.5.

There are two sets of experiments; the experiments of one bundle, and the crossing of two bundles.

In the case of single bundle tests with MRI signals, we take the same approach as the histogram framework. We fix all the parameters of (4.7) but $D_{\perp}$.

For the crossing bundles, we begin by doing two Zeppelin fittings by fixing first θ and then α. We do the same using a Zeppelin + Stick model, but fixing f on the two searches. Finally, we do a Zeppelin + Stick search just fixing $D_{\parallel}$.

TABLE 4.5: Degrees of freedom of each model.

Model	Degrees of Freedom
Zeppelin for each compartment	$D_{\perp}$
Zeppelin for one bundle	$D_{\perp}$
Zeppelin + Stick for one bundle	$D_{\perp}$
Zeppelin for two bundles	$D_{\parallel}$, $D_{\perp}$, θ , α
Zeppelin + Stick for two bundles	$D_{\parallel}$, $D_{\perp}$, θ , α , f

4.5 Modelling error in the coarse graining regime

This section will analyze the theoretical behavior of the error deviation in some special cases.

4.5.1 Fitting a single tensor to a two-compartment substrate signal

In a bi-compartment Gaussian model, the EAP can be viewed as a mixture of two zero-mean multivariate normal distributions, each one characterized by their ICVF weight, and their covariance matrix (directly related to the diffusion tensor by $\mathbf{\Sigma} = 2\Delta\boldsymbol{D}$). If one were to fit this mixture model to the bicompartment substrate, comparison between the parameters would be direct. However, in the case which one were to use classic DTI

with only one tensor, this comparison would not be as straightforward as the previous case. To compare the ground truth propagator between to the proposed single tensor model, we propose the Kullback-Liebler Divergence (KLD). Unfortunately, the KLD is analytically intractable for Gaussian Mixtures (Hershey and Olsen, 2007). Instead, we propose to calculate a lower bound based on the work of Durrieu, Thiran, and Kelly, 2012.

Let G_{GT} be the propagator of the ground truth model, which is a multicompartment model in the form of a mixture of two Gaussian zero mean $\mathcal{G}_{GT,Intra}, \mathcal{G}_{GT,Extra}$; covariance matrices $\mathbf{\Sigma}_{GT,Intra}, \mathbf{\Sigma}_{GT,Extra}$; and ICVF $w_{GT,Intra} = f$ and $w_{GT,Intra} = 1 - f$. Let $\hat{G}$ be the estimated propagator, in the form a single Gaussian distribution with zero mean $\hat{\mathcal{G}}$, and covariance matrix $\hat{\mathbf{\Sigma}}$. The distribution has no ICVF weighting, so the weight $\hat{w}$ of $\hat{\mathcal{G}}$ would be just 1. We propose the following form,

$$D_{KL}(G_{GT}||\hat{G}) \geq \sum_{C_1}^{\{Intra,Extra\}} w_{GT,C_1} \log \frac{\sum_{C_2}^{\{Intra,Extra\}} w_{GT,C_2} \exp[-D_{KL}(\mathcal{G}_{GT,C_1}||\mathcal{G}_{GT,C_2})]}{t_{C_1,\hat{G}}} - \frac{w_{GT,C_1}}{2}\mathcal{H}(\mathcal{G}_{GT,C_1}), \quad (4.16)$$

were $D_{KL}(a||b)$ is the KLD between distributions a and b, $\mathcal{H}(a)$ is the entropy of distribution a, and $t_{C_1,\hat{G}}$ is a normalization constant (refer to Durrieu, Thiran, and Kelly, 2012). By removing the two cases of the denominator in which the divergence is calculated for equal distributions (in which case the result is 0), the expression becomes

$$D_{KL}(G_{GT}||\hat{G}) \geq \sum_{C_1}^{\{Intra,Extra\}} w_{GT,C_1} \log \frac{w_{GT,\neg C1} \exp[-\frac{1}{2}\log\frac{\mathbf{\Sigma}_{GT,\neg C_1}}{\mathbf{\Sigma}_{GT,C_1}} - \frac{1}{2}\operatorname{Tr}(\mathbf{\Sigma}_{GT,\neg C_1}^{-1}\mathbf{\Sigma}_{GT,C_1}) + \frac{3}{2}]}{\exp[-\frac{3}{2}\log(2\pi) - \frac{1}{2}\log\det(\mathbf{\Sigma}_{GT,C_1} + \hat{\mathbf{\Sigma}})]} - \frac{w_{GT,C_1}}{2}\log[(2\pi e)^3 \det(\mathbf{\Sigma}_{GT,C1})]. \quad (4.17)$$

Here, $\neg C_1$ denotes the opposite compartment of C_1. So, if C_1 references to the *Intra* compartment, $\neg C_1$ will reference to *Extra*, and vice versa.

4.5.2 Orthogonal diffusion using Zeppelin-Stick

The MRI signals are additive, which means the diffusion contribution of two compartments is also additive. Imagine a fitting experiment in a substrate with two compartments. We want to estimate the orthogonal diffusion. For the sake of consistence, lets define the diffusion coefficient of one restricted compartment as $D_{\perp,Intra}$ and the outer compartment as $D_{\perp,Extra}$. The volume fraction between them is f. This means the substrate orthogonal diffusion is the sum of both coefficients weighed by the ICVF. Let $D_\perp$ be

$$D_\perp = fD_{\perp,Intra} + (1-f)D_{\perp,Extra}. \quad (4.18)$$

We call this the *ground truth*. Now, imagine we obtained estimated measures of these parameters. Let the estimated parameters be $\hat{D}_{\perp,Intra}$, $\hat{D}_{\perp,Extra}$ and $\hat{f}$. The total estimated diffusion $\hat{D}_\perp$ is computed as formerly. Now, lets define the relative error between the

predicted and the real total orthogonal diffusion,

$$\varepsilon(\hat{D}_\perp) = \frac{\hat{D}_\perp - D_\perp}{D_\perp}. \tag{4.19}$$

Normally, ε is expressed as a percentage by multiplying it by 100%, which means, for example, a value of 0.5 means 50% of deviation form the real value. Note that the error can also be negative, implying a negative deviation from the ground truth. Assume a perfect estimation of the ICVF and *Extra* orthogonal diffusion, so $\hat{D}_{\perp,Extra} = D_{\perp,Extra}$ and $\hat{f} = f$. In the case of Zeppelin-Stick, the *Intra* orthogonal diffusion is neglected, so assume $\hat{D}_{\perp,Intra} = 0$. The substitution of (4.18) for both the estimated and real diffusion in (4.19), and dividing both parts of the fraction by $D_{\perp,Intra}$ yields

$$\epsilon(\hat{D}_\perp) = \frac{-f}{f + (1-f)\frac{D_{\perp,Extra}}{D_{\perp,Intra}}}. \tag{4.20}$$

The first insight is on the sign of the numerator. All parameters are positive, which means the model will exclusively underestimate, not overestimate. Zeppelin-Stick model assumption of negligible $D_{\perp,Intra}$ means that $D_{\perp,Intra} << D_{\perp,Extra}$, so the ratio between $D_{\perp,Extra}$ and $D_{\perp,Intra}$ in the denominator of (4.20) should be significantly greater than 1, the maximum value f could take. For low values of f, the part weighted by $(1-f)$, the ratio of coefficients, dominates. This means the error stays very low, because the ratio is significantly bigger than any value the numerator of (4.20). As f grows, the error depends on how big is $D_{\perp,Extra}$ compared to $D_{\perp,Intra}$. If is orders of magnitude bigger, there should be no worries, as an ICVF greater than 0.9 is very rare. If it is not big enough, a notable error could arise. When $f \to 1$, the error will tend to 1. This is obvious, as an ICVF of 1 means there is no *Extra* diffusivity, and estimating an orthogonal diffusion of zero for a non-zero ground truth means we have a 100% error.

4.6 Histogram Fitting: An Intuition On Orthogonal Diffusivity

Our first proposed approach is to directly fit a normal distribution to the pseudo displacement vector set in (4.4), in order to obtain insights on the shape of the diffusion propagator (assuming the normality of DTI). We did this in one dimension. While the next approach is generalizable to 3 dimensions, we found results do not explain further than a one dimensional case.

We opted to do histogramming because is the simplest method to estimate the density, having to set just one parameter, the bin size. Other methods, such as Kernel Density Estimation, have more parameters to tune. Another idea is the use of a multivariate normality test, such as Mardia, Henze-Zirkler, Shapiro-Wilk, graphical methods, and others (Korkmaz, Goksuluk, and Zararsiz, 2014) (Porras-Cerron, 2016). However, this is not directly applicable to the whole bundle, because we have the same number of spins for extra and intra-axonal. In a real substrate, the proportion of molecules is weighted by the ICVF. As previously stated, taking a varying proportion of spins from each compartment would also affect the quality of the signal proportional to the spins in a given compartment.

TABLE 4.6: Parameters of the histogram.

Parameter		Value
N_{bin}	Number of bins	224
Δh	Width of bin	1/3 µm
	Lower limit of the first bin	−74.6 µm
	Upper limit of the last bin	74.6 µm

We define the histogram $\boldsymbol{h}_i^c$ as the binning of the projection of the 3-dimensional displacement in the x axis. The superindex c denotes the compartment, intra-axonal or extra-axonal. The subindex i denotes the value at the i-th bin. We choose this direction because we assume radial symmetry, which means the orthogonal diffusion is the same along any direction on the xy plane. We choose heuristically the resolution of the histogram, the number of bins N_{bin}, as a trade-off between size complexity and resolution. The size of the histogram is set in such way we only discard at most 1% of the spins to preserve statistical power.

Next, the histogram is converted to a Discrete Probability Distribution (DPD), in which the value at each bins maps directly to the probability of having a displacement of that magnitude and direction. This is done by dividing each bin height by the sum of all elements in the histogram. Let C be a random binary variable. It takes the value of 1 when a given spin is located in intra-axonal space, and 0 when is in extra-axonal space. It follows that $\Pr(C = 1) = f$ and $\Pr(C = 0) = 1 - f$. We define the operator $[\cdot]$ as a function which discretizes the position along the x axis and returns the indices for $\boldsymbol{h}_i$. We define the DPD as a conditional discrete probability distribution, taking the discretization of x as a random variable.

$$\Pr([x] \mid C) = \frac{\boldsymbol{h}^C_{[x]}}{\sum_i \boldsymbol{h}^C_i}. \tag{4.21}$$

Thus, it is possible to define the probability density function of the complete bundle (i.e. the density function of the intra and extra-axonal compartments together) by the law of total probability.

$$\begin{aligned}\Pr([x]) &= \Pr(C = 1)\Pr([x] \mid C = 1) + \Pr(C = 0)\Pr([x] \mid C = 0) \\ &= f\frac{\boldsymbol{h}^{intra}_{[x]}}{\sum_i \boldsymbol{h}^{intra}_i} + (1 - f)\frac{\boldsymbol{h}^{extra}_{[x]}}{\sum_i \boldsymbol{h}^{extra}_i}.\end{aligned} \tag{4.22}$$

4.6.1 Fitting Procedure

A zero-centered Gaussian distribution is fitted to the discrete distributions of the distribution of the two compartments and the whole bundle using two norms. Let Δh be the bin width and $\overline{\boldsymbol{h}}$ be the vector of the centers of all the bins. Let $\|\boldsymbol{v}\|_2 = \sqrt{\boldsymbol{v}^T\boldsymbol{v}}$ be the Euclidean or L_2 norm of vector $\boldsymbol{v}$.

$$\underset{\sigma^2}{\operatorname{argmin}} \left\| \Pr(\overline{\boldsymbol{h}})/\Delta h - \boldsymbol{p}(\overline{\boldsymbol{h}}, \sigma^2) \right\|_1 \tag{4.23}$$

$$\underset{\sigma^2}{\operatorname{argmin}} \left\| \Pr(\bar{\boldsymbol{h}})/\Delta h - \boldsymbol{p}(\bar{\boldsymbol{h}}, \sigma^2) \right\|_2 \tag{4.24}$$

The probability is divided by the bin width to rescale the histogram, so we reinterpret it as a piece-wise continuous probability density. In this way, we are able to compare it with other continuous densities.

$$\int_{\bar{h}_1 - \Delta h/2}^{\bar{h}_{N_{bin}} + \Delta h/2} \frac{\Pr([x])}{\Delta h} dx = 1.$$

The function $\boldsymbol{p}(\bar{\boldsymbol{h}}, \sigma^2)$ computes the probability value for each of the bins by integrating along its limits. For this experiment, a simple trapezoidal approximation is used,

$$p_i = \frac{\Delta h}{2}[g_{0,\sigma^2}(\bar{h}_i - \Delta h/2) + g_{0,\sigma^2}(\bar{h}_i + \Delta h/2)], \tag{4.25}$$

where $g_{\mu,\sigma^2}(x)$ is the density of a Gaussian with mean μ and variance σ^2 evaluated at x.

4.6.2 Variance Fitting in Histograms

For each simulation of interest, four histograms are computed for intra-axonal, extra-axonal, the whole bundle, and the smoothed whole bundle. We smoothed out the whole bundle histogram in an attempt to compensate for the low resolution in the intra-axonal part. We believe the intra-axonal histograms concentrates most of the variance information near the center, so smoothing could compensate for this. The smoothing was done convolving the original histogram with a Gaussian kernel with bandwitdh of 6.6 bins. This was chosen heuristically, as it was the best in terms of accuracy in prediction. We histogrammed the projections of the displacement vectors along an orthogonal direction to the main diffusion axis. We assume the diffusion is equal along any direction in the xy plane, so we arbitrarily chose the x axis. We are particularly interested in this direction because non Gaussianity is visible the most on the radial diffusion component of the total bundle. This is because the highly restricted orthogonal diffusion of the intra-axonal compartment has a "spike" of spins with very small displacement afar from the origin in the orthogonal directions. In order to solve (4.23) and (4.24), a local grid search is performed along the variance σ^2 with $N_{grid} = 1000$ and $\epsilon = 99.9\%$. Then, we compare the relative error between the fitted $\hat{\sigma}^2$ and the variance of the histogram. The variance should correspond directly with the mean squared displacement in one dimension (2.7), so it is possible to infer the diffusion coefficient from σ^2. We fitted the distribution to the intra-axonal, extra-axonal and total displacement histograms.

The extra-axonal diffusion is anisotropic, but is majorly Gaussian, just as can be seen with small estimation errors in table 4.7. The intra-axonal histogram looks like a spike, and fitting has a limited success with an error between $25\% - 30\%$. The most interesting case is when the histograms are mixed to form the total diffusion probability estimation. Different overall behaviors can be distinguished between L_1 (4.23) and L_2 (4.24) experiments. For low f values, the Gaussian tends to fit the extra-axonal contribution better, which would correspond with the tails of the histogram. The fitted distribution becomes nearer to the peak of the intra-axonal displacement as the ICVF f grows. The difference between the two metrics is more notorious in the smoothed out histogram. The solution of the problem with L_2 norm prefers to fit the peak, while L_1 norm has a better balance

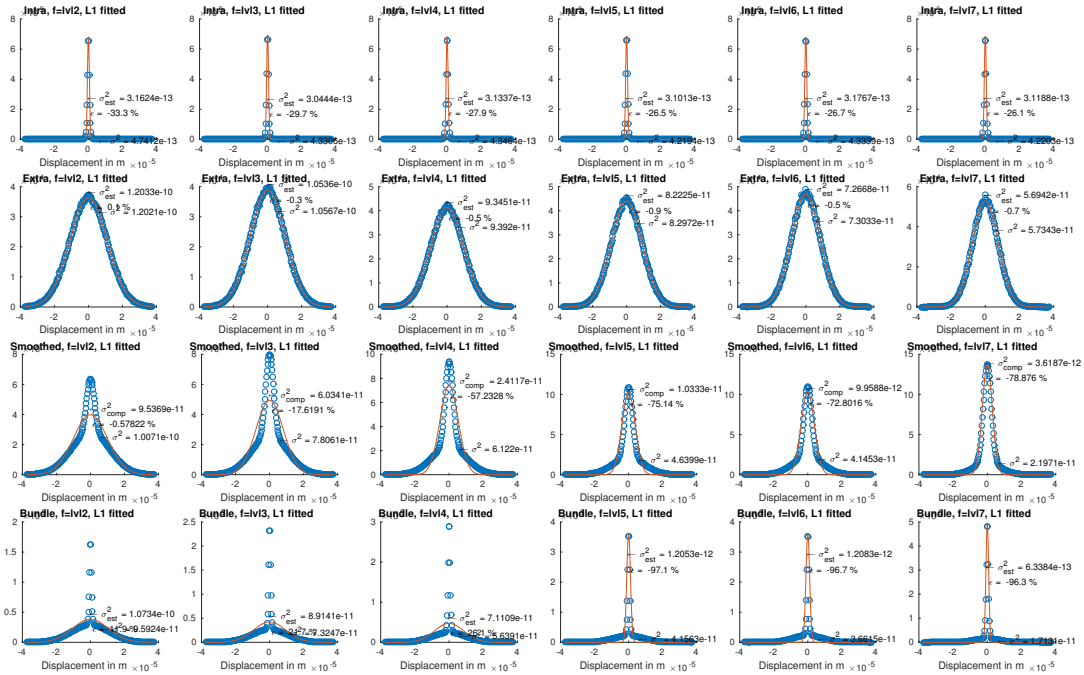

FIGURE 4.4: One dimension fitting for problem (4.23) (L_1 norm) for whole bundles with different levels of f. Blue points correspond to the histogram, the red corresponds with the fitted distribution.

between intra and extra. Another fact is the smoothing of the histogram improved the estimation quality. This is a good technique to deal with the low resolution of the peak.

TABLE 4.7: Results of one-dimensional Histogram Fitting Experiment for problem (4.23) (L_1 norm), and (4.24) (L_2 norm). The table shows the relative errors between the fitted $\hat{\sigma}^2$ for each bundle and the respective ground truth.

Metric f	Extra		Intra		Bundle		Smoothed	
	L_1	L_2	L_1	L_2	L_1	L_2	L_1	L_2
lvl2	0.10%	0.10%	-33.30%	-30.90%	11.90%	-37.70%	-0.58%	-32.08%
lvl3	-0.30%	-0.50%	-29.70%	-27.50%	21.70%	-68.70%	-17.62%	-51.51%
lvl4	-0.50%	-1.10%	-27.90%	-25.30%	26.10%	-92.70%	-57.23%	-65.27%
lvl5	-0.90%	-1.10%	-26.50%	-24.10%	-97.10%	-96.50%	-75.14%	-74.47%
lvl6	-0.50%	-1.10%	-26.70%	-24.30%	-96.70%	-95.90%	-72.80%	-72.12%
lvl7	-0.70%	-1.70%	-26.10%	-23.50%	-96.30%	-96.50%	-78.88%	-79.39%
Mean	**-0.47%**	-0.90%	-28.37%	**-25.93%**	**-38.40%**	-81.33%	**-50.37%**	-62.47%

Chapter 5

Results And Discussion

5.1 One Dimensional Fitting

We solve (4.6) fitting for a single non-crossing bundle aligned to z. We are interested in the non-Gaussian diffusion direction, so we fixed all the parameters of the model, but $D_\perp$. A local grid search was performed along this parameter using $N_{grid} = 200,000$ and $\epsilon = 99.9\%$. This follows the same logic as the 1-d histogram search, by only sweeping the parameter responsible of the non Gaussian part of the diffusion. The search is done in the two compartments, as well as the whole bundle. The two separated compartments are fitted just using the zeppelin model, while the whole bundle is fitted with the zeppelin and zeppelin-stick variants.

As can be observed in table 5.1, the extra-axonal part of the diffusion is easy to estimate, and the search underestimates with small error. As for the intra-axonal diffusion, it looks like the search cannot reach a minimum within the neighborhood (see figure 5.1). The distance function keeps decreasing for smaller values of the estimated diffusion coefficient $\hat{D}_\perp$. It is possible the model cannot represent very low diffusivity, and the best option is actually $\hat{D}_\perp = 0$ (a stick). In the case of the total signal, we can see an important underestimation fitting the zeppelin.

There is a clear underestimation for all ICVF levels in the case of the whole bundle fitting using just the zeppelin. The underestimation deviates further away as the ICVF increases for almost all levels of f. However, the substrate with the greatest ICVF (lvl7) is estimated with better accuracy than the next smaller one. This might find an explanation based on the same mechanics of the histogram fitting. We hypothesize this is because the very low $D_{\perp,intra}$ (refer to table 4.4) starts to dominate. A similar trend is seen in the results of the normal total bundle histogram fitting at table 4.7.

The Zeppelin + Stick model is superior to the simple zeppelin by a notable margin, as the estimation error never surpasses 7% of the nominal value. The error follows a decreasing trend in the same manner as the simple zeppelin. By taking the off the burden of explaining the restricted intra-axonal diffusion from the zeppelin part of the model, the part is free to fit just the extra-axonal part of the bundle, which is almost Gaussian. One important distinction should be noted in the case of the stick-zeppelin experiment. The estimated coefficient $\hat{D}_\perp$ is plugged in (4.12) and then, its contribution is weighted by $(1 - f)$ in (4.13). This means the correct ground truth to compare with is the $D_\perp$ of just the extra-axonal diffusion, not of the total bundle as computed in (4.5).

TABLE 5.1: Results of MRI Model Fitting Experiment. The table shows the relative error between the predicted $\hat{D}_\perp$ for each bundle and the respective ground truth.

f	Extra (Zeppelin)	Intra (Zeppelin)	Bundle (Zeppelin)	Bundle (Zeppelin + Stick)
lvl2	-4.85%	-99.90%	-22.62%	-5.28%
lvl3	-4.88%	-99.90%	-26.07%	-5.22%
lvl4	-5.12%	-99.90%	-27.79%	-5.87%
lvl5	-4.94%	-99.90%	-28.85%	-5.80%
lvl6	-5.17%	-99.90%	-29.20%	-6.29%
lvl7	-5.04%	-99.90%	-27.61%	-6.95%

5.2 One Crossing with 3 Degrees Of Freedom

For each f dataset, we create 4 extra bundles rotated 60, 70, 80 and 90 degrees from z, thus, we have 24 crossings in total. A grid search is performed to fit a Zeppelin (4.7) and a Zeppelin-Stick (4.13) using (4.6) for 3 degrees of freedom to characterize the effect of knowing beforehand a subset of the parameters. We try to do the fitting by using the acquisition obtained with the one shell scheme.

5.2.1 3 degrees of freedom: $\alpha, D_\parallel, D_\perp$

We fix the value of θ and search along $D_\parallel, D_\perp$ and α using $N_{grid} = 100$ for all the parameters. The mixing factor estimation for the two models, as well as the parallel diffusion estimation, is very near to the ground truth. This can be seen in table 5.2. In the case of the predicted orthogonal coefficient fitting the zeppelin, we note a increasing trend in the underestimation magnitude in figure 5.2 dependent of the ICVF of the substrate. The underestimation does not appear to be correlated to the angle of rotation in the ground truth, as can be seen in the same figure. This behavior is predicted by the fitting in one dimension, as the one compartment model cannot represent the diffusion in a whole bundle. This changes when the zeppelin + stick model is fitted. We have perfect α estimation, and small subestimation of $D_\parallel$ and $D_\perp$. Curiously, the subestimation error is similar for all the levels of f and rotation angles. It looks like the model is almost enough to represent the signal to a high degree, and this bias is inherent to the model. We could do further statistical validation with other substrates in order to verify if it is feasible to compensate for this error, and obtain a perfect prediction.

5.2.2 3 degrees of freedom: $\theta, D_\parallel, D_\perp$

Now, we fix the value of α instead of θ, and search along $D_\parallel, D_\perp$ and θ using $N_{grid} = 100$ for all the parameters, in the same fashion as the former search. The prediction error of $\hat{\theta}$ is zero for the majority of cases. The mix factor α is fixed, which means it has zero deviation. The former implies both of the 3 DOF searches have very low errors on the prediction of $\hat{\theta}$ and $\hat{\alpha}$. Therefore, the results for the rest of the predicted variables are practically the same, for the exception of some values (refer to table 5.3 an figure 5.3). The same conclusions of the former experiment apply for the two models.

TABLE 5.2: Results of first 3 DOF search fitting $\alpha, D_{\parallel}, D_{\perp}$. The table shows the relative error between the predicted parameters of the fiber cross and their respective ground truth.

Zeppelin				
f	θ	$\varepsilon(\hat{D}_{\parallel})$	$\varepsilon(\hat{D}_{\perp})$	$\varepsilon(\hat{\alpha})$
lvl2	60.00	2.00%	-23.98%	0.00%
	70.00	2.00%	-23.98%	0.00%
	80.00	4.00%	-23.98%	0.00%
	90.00	4.00%	-23.98%	0.00%
lvl3	60.00	0.00%	-25.97%	0.00%
	70.00	0.00%	-25.97%	0.00%
	80.00	0.00%	-25.97%	0.00%
	90.00	0.00%	-25.97%	0.00%
lvl4	60.00	0.00%	-27.97%	0.00%
	70.00	0.00%	-27.97%	0.00%
	80.00	0.00%	-27.97%	0.00%
	90.00	0.00%	-27.97%	0.00%
lvl5	60.00	-2.00%	-27.97%	0.00%
	70.00	-2.00%	-27.97%	0.00%
	80.00	-2.00%	-27.97%	0.00%
	90.00	0.00%	-29.97%	0.00%
lvl6	60.00	-2.00%	-27.97%	0.00%
	70.00	-2.00%	-27.97%	0.00%
	80.00	0.00%	-29.97%	0.00%
	90.00	0.00%	-29.97%	0.00%
lvl7	60.00	-2.00%	-25.97%	0.00%
	70.00	-2.00%	-25.97%	0.00%
	80.00	-2.00%	-27.97%	0.00%
	90.00	-2.00%	-27.97%	0.00%

Zeppelin + Stick				
f	θ	$\varepsilon(\hat{D}_{\parallel})$	$\varepsilon(\hat{D}_{\perp})$	$\varepsilon(\hat{\alpha})$
lvl2	60.00	-4.00%	-4.00%	0.00%
	70.00	-4.00%	-4.00%	0.00%
	80.00	-4.00%	-4.00%	0.00%
	90.00	-4.00%	-4.00%	0.00%
lvl3	60.00	-4.00%	-4.00%	0.00%
	70.00	-4.00%	-4.00%	0.00%
	80.00	-4.00%	-4.00%	0.00%
	90.00	-4.00%	-4.00%	0.00%
lvl4	60.00	-4.00%	-2.00%	0.00%
	70.00	-4.00%	-2.00%	0.00%
	80.00	-4.00%	-2.00%	0.00%
	90.00	-4.00%	-2.00%	0.00%
lvl5	60.00	-4.00%	-2.00%	0.00%
	70.00	-4.00%	-2.00%	0.00%
	80.00	-4.00%	-2.00%	0.00%
	90.00	-4.00%	-2.00%	0.00%
lvl6	60.00	-4.00%	-2.00%	0.00%
	70.00	-4.00%	-2.00%	0.00%
	80.00	-2.00%	-5.99%	0.00%
	90.00	-2.00%	-5.99%	0.00%
lvl7	60.00	-4.00%	0.00%	0.00%
	70.00	-4.00%	-2.00%	0.00%
	80.00	-4.00%	-2.00%	0.00%
	90.00	-4.00%	-2.00%	0.00%

TABLE 5.3: Results of first 3 DOF search fitting $\theta, D_{\parallel}, D_{\perp}$. The table shows the relative error between the predicted parameters of the fiber cross and their respective ground truth.

Zeppelin				
f	θ	$\varepsilon(\hat{D}_{\parallel})$	$\varepsilon(\hat{D}_{\perp})$	$\varepsilon(\hat{\theta})$
lvl2	60.00	2.00%	-23.98%	2.00%
	70.00	4.00%	-23.98%	2.00%
	80.00	4.00%	-23.98%	2.00%
	90.00	4.00%	-23.98%	0.00%
lvl3	60.00	0.00%	-25.97%	-0.00%
	70.00	0.00%	-25.97%	0.00%
	80.00	0.00%	-25.97%	0.00%
	90.00	0.00%	-25.97%	0.00%
lvl4	60.00	0.00%	-27.97%	-0.00%
	70.00	0.00%	-27.97%	0.00%
	80.00	0.00%	-27.97%	0.00%
	90.00	0.00%	-27.97%	0.00%
lvl5	60.00	-2.00%	-27.97%	-0.00%
	70.00	-2.00%	-27.97%	0.00%
	80.00	-2.00%	-27.97%	0.00%
	90.00	0.00%	-29.97%	0.00%
lvl6	60.00	-2.00%	-27.97%	-0.00%
	70.00	-2.00%	-27.97%	0.00%
	80.00	0.00%	-29.97%	0.00%
	90.00	0.00%	-29.97%	0.00%
lvl7	60.00	-2.00%	-25.97%	-0.00%
	70.00	-2.00%	-25.97%	0.00%
	80.00	-2.00%	-27.97%	0.00%
	90.00	-2.00%	-27.97%	0.00%

Zeppelin + Stick				
f	θ	$\varepsilon(\hat{D}_{\parallel})$	$\varepsilon(\hat{D}_{\perp})$	$\varepsilon(\hat{\theta})$
lvl2	60.00	-4.00%	-4.00%	-0.00%
	70.00	-4.00%	-4.00%	0.00%
	80.00	-4.00%	-4.00%	0.00%
	90.00	-4.00%	-4.00%	0.00%
lvl3	60.00	-4.00%	-4.00%	-0.00%
	70.00	-4.00%	-4.00%	0.00%
	80.00	-4.00%	-4.00%	0.00%
	90.00	-4.00%	-4.00%	0.00%
lvl4	60.00	-4.00%	-2.00%	-0.00%
	70.00	-4.00%	-2.00%	0.00%
	80.00	-4.00%	-2.00%	0.00%
	90.00	-4.00%	-2.00%	0.00%
lvl5	60.00	-4.00%	-2.00%	-0.00%
	70.00	-4.00%	-2.00%	0.00%
	80.00	-4.00%	-2.00%	0.00%
	90.00	-4.00%	-2.00%	0.00%
lvl6	60.00	-4.00%	-2.00%	-0.00%
	70.00	-4.00%	-2.00%	0.00%
	80.00	-2.00%	-5.99%	0.00%
	90.00	-2.00%	-5.99%	0.00%
lvl7	60.00	-4.00%	0.00%	-0.00%
	70.00	-4.00%	-2.00%	0.00%
	80.00	-4.00%	-2.00%	0.00%
	90.00	-4.00%	-2.00%	0.00%

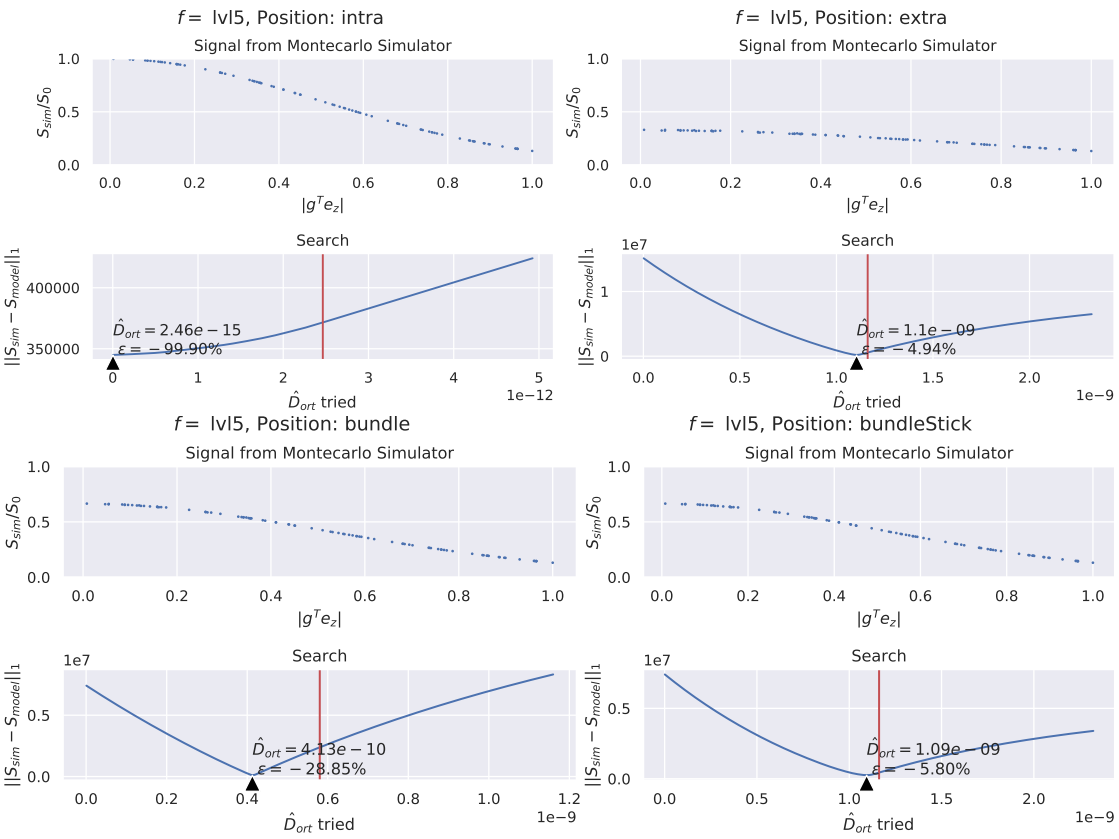

FIGURE 5.1: Example of one-dimension fitting DTI zeppelin and zeppelin stick models with relative prediction error ε against ground truth. The top plot is the normalized measured signal, ordered by orthogonality to the z axis. The second one is the norm as a function of the estimated parameter. Red line on the middle shows ground truth.

5.3 One crossing with 4 Degrees Of Freedom

This is the most challenging test for the stick and zeppelin model. There is an important problem in the contribution of the Zeppelin in the fitting of the extra-axonal compartment. When using only a single non zero b-value, a decrease in the signal on one of the compartments in a bundle can be compensated by the other varying f and $D_\perp$. In fact, this makes the problem ill-posed in the sense of Hadamard if the MRI protocol has just one shell (Scherrer and Warfield, 2010) (Scherrer and Warfield, 2012) (Jelescu, Veraart, et al., 2016). We demonstrate this by doing a grid search on $\alpha, \theta, D_\perp, f$ with $N_{grid} = 50$ for all parameters. Figure 5.4 shows the countour plot of the normalized distance function (4.6). We did the search and fixed $\hat{\alpha}$ and $\hat{\theta}$ to their ground truths. The function has a valley, so there is not an unique solution. The algorithm tends to choose a small ICVF f. In this way, all the orthogonal diffusion is mostly controlled by the extra-axonal part because is weighted by $1 - f$ (see table 5.4). Consequently, the quality of the estimation worsens as the ground truth f increases, because the intra-axonal contribution begins to dominate (see figure 5.5).

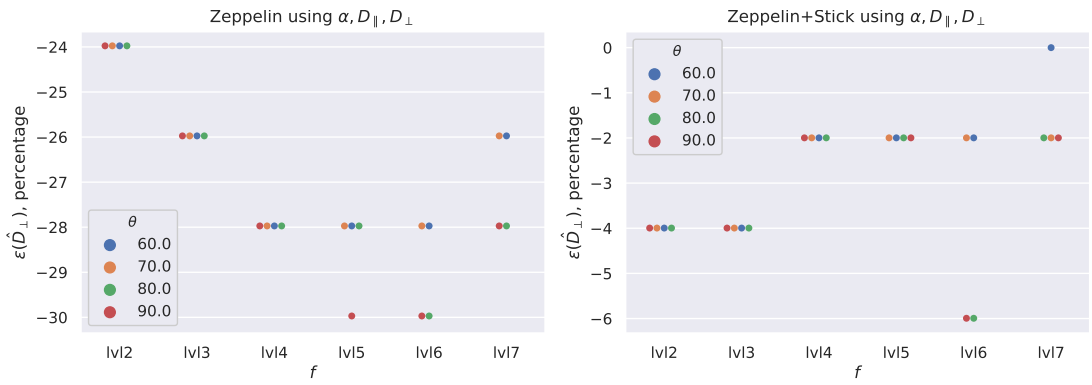

FIGURE 5.2: Orthogonal Coefficient error in 3 DOF Search using $\alpha, D_{\parallel}, D_{\perp}$.

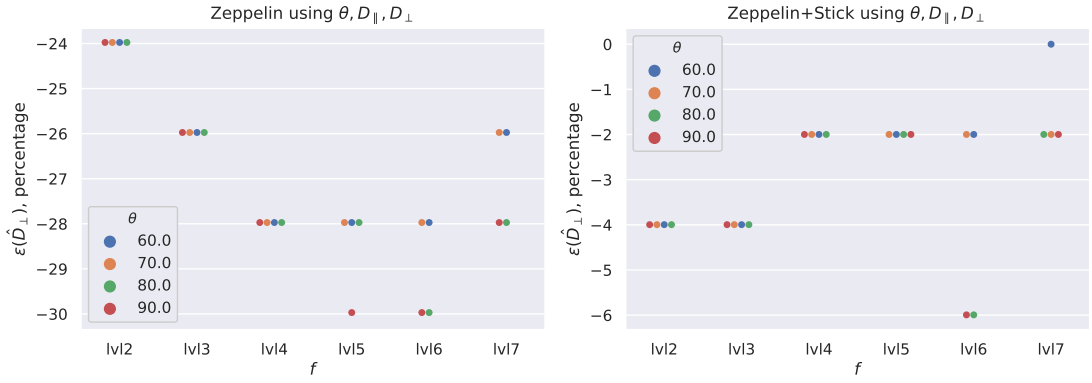

FIGURE 5.3: Orthogonal Coefficient error in 3 DOF Search using $\theta, D_{\parallel}, D_{\perp}$.

Finally, we repeat the same 4 DOF experiment, now, but now using the 4-shell signals. The accuracy of prediction improves dramatically, as the mix factor α, the rotation angle θ, and the ICVF f are retrieved perfectly in most of the cases. The only factor presenting a bias is the orthogonal diffusion coefficient $D_{\perp}$. The underestimation error is constant for the first 4 levels of ICVF, and increases for the last two. There is a worsening effect mediated by f, but it does not have a clear pattern such as in the last experiment. In comparison to Figure 5.4, the contour plots of the distance surface in this experiment have a defined minimum, but a similar shape (Figure 5.7).

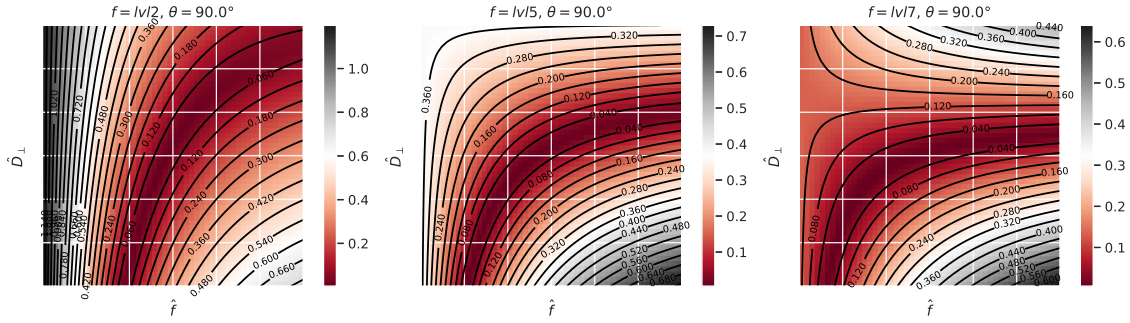

FIGURE 5.4: Contour plots of 4DOF $\|S_{sim} - S_{model}\|_1 \,/\, \|S_{sim}\|_1$ with $D_\parallel, \alpha, \theta$ fixed to ground truth. Experiment with one shell.

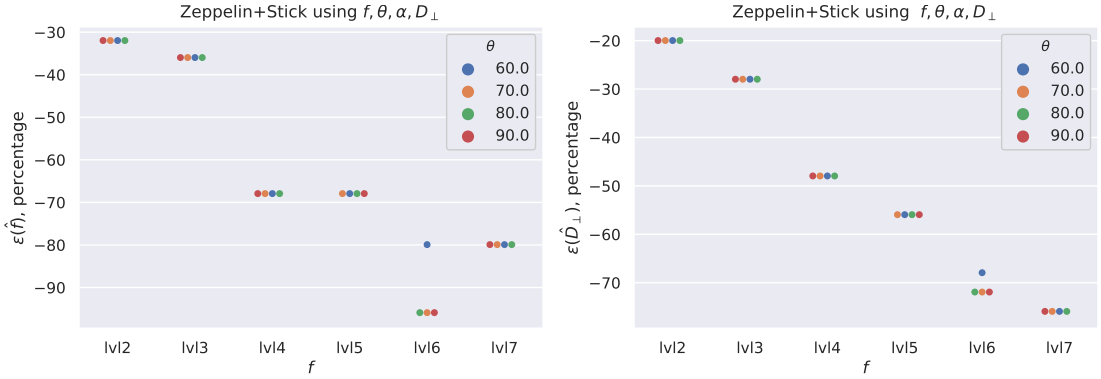

FIGURE 5.5: Volume fraction and orthogonal Coefficient and errors in 4 DOF Search with one shell.

FIGURE 5.6: Volume fraction and orthogonal Coefficient and errors in 4 DOF Search with four shells.

TABLE 5.4: Results of 4DOF search using Zeppelin + Stick with one shell. The table shows the relative error between the predicted parameters for each bundle and the respective ground truth.

f	θ	$\varepsilon(\hat{f})$	$\varepsilon(\hat{D}_\perp)$	$\varepsilon(\hat{\alpha})$	$\varepsilon(\hat{\theta})$
lvl2	60.00	-31.97%	-19.98%	4.00%	4.00%
	70.00	-31.97%	-19.98%	0.00%	0.00%
	80.00	-31.97%	-19.98%	0.00%	0.00%
	90.00	-31.97%	-19.98%	0.00%	0.00%
lvl3	60.00	-35.96%	-27.97%	0.00%	-0.00%
	70.00	-35.96%	-27.97%	0.00%	0.00%
	80.00	-35.96%	-27.97%	0.00%	0.00%
	90.00	-35.96%	-27.97%	0.00%	0.00%
lvl4	60.00	-67.93%	-47.95%	0.00%	-0.00%
	70.00	-67.93%	-47.95%	0.00%	0.00%
	80.00	-67.93%	-47.95%	0.00%	0.00%
	90.00	-67.93%	-47.95%	0.00%	0.00%
lvl5	60.00	-67.93%	-55.94%	0.00%	-0.00%
	70.00	-67.93%	-55.94%	0.00%	0.00%
	80.00	-67.93%	-55.94%	0.00%	0.00%
	90.00	-67.93%	-55.94%	0.00%	0.00%
lvl6	60.00	-79.92%	-67.93%	0.00%	-0.00%
	70.00	-95.90%	-71.93%	0.00%	0.00%
	80.00	-95.90%	-71.93%	0.00%	0.00%
	90.00	-95.90%	-71.93%	0.00%	0.00%
lvl7	60.00	-79.92%	-75.92%	0.00%	-0.00%
	70.00	-79.92%	-75.92%	0.00%	0.00%
	80.00	-79.92%	-75.92%	0.00%	0.00%
	90.00	-79.92%	-75.92%	0.00%	0.00%

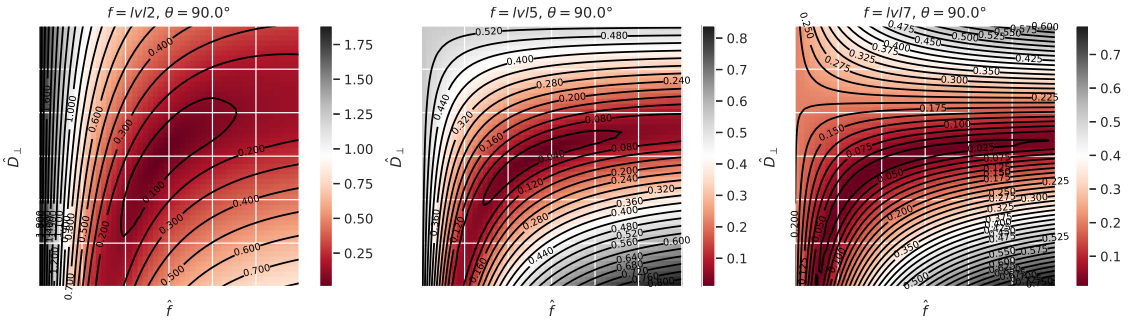

FIGURE 5.7: Contour plots of 4DOF $\|S_{sim} - S_{model}\|_1 \,/\, \|S_{sim}\|_1$ with $D_\parallel, \alpha, \theta$ fixed to ground truth. Experiment with four shells.

TABLE 5.5: Results of 4DOF search using Zeppelin + Stick with four shells. The table shows the relative error between the predicted parameters for each bundle and the respective ground truth.

f	θ	$\varepsilon(\hat{f})$	$\varepsilon(\hat{D}_{\perp})$	$\varepsilon(\hat{\alpha})$	$\varepsilon(\hat{\theta})$
lvl2	60.00	4.00%	-4.00%	0.00%	-0.00%
	70.00	-0.00%	-7.99%	0.00%	0.00%
	80.00	-0.00%	-7.99%	0.00%	0.00%
	90.00	-0.00%	-7.99%	0.00%	0.00%
lvl3	60.00	0.00%	-7.99%	0.00%	-0.00%
	70.00	0.00%	-7.99%	0.00%	0.00%
	80.00	0.00%	-7.99%	0.00%	0.00%
	90.00	0.00%	-7.99%	0.00%	0.00%
lvl4	60.00	0.00%	-7.99%	0.00%	-0.00%
	70.00	0.00%	-7.99%	0.00%	0.00%
	80.00	0.00%	-7.99%	0.00%	0.00%
	90.00	0.00%	-7.99%	0.00%	0.00%
lvl5	60.00	0.00%	-7.99%	0.00%	-0.00%
	70.00	0.00%	-7.99%	0.00%	0.00%
	80.00	0.00%	-7.99%	0.00%	0.00%
	90.00	0.00%	-7.99%	0.00%	0.00%
lvl6	60.00	0.00%	-7.99%	0.00%	-0.00%
	70.00	0.00%	-11.99%	0.00%	0.00%
	80.00	0.00%	-11.99%	0.00%	0.00%
	90.00	0.00%	-11.99%	0.00%	0.00%
lvl7	60.00	0.00%	-11.99%	0.00%	-0.00%
	70.00	0.00%	-11.99%	0.00%	0.00%
	80.00	0.00%	-11.99%	0.00%	0.00%
	90.00	0.00%	-11.99%	0.00%	0.00%

Chapter 6

Conclusion

We have explored the effects of non Gaussianity of hindered diffusion on some DTI-based models of white matter. The used substrate grossly simplifies the complexity of microstructure inside the brain. Real axons are partially permeable; have intricate structure, such as Ranvier nodes and interactions with glia. They also have undulations and discontinuities. And all of this do not take into account all the abnormalities a pathological sample of white matter might have. By doing these experiments on a simplified model with several strong assumptions and simplifications, we have bounded the deviation of the estimated parameters from the real ones. Using the same methodology on real acquisitions from machines scanning real brains will not improve the fitting error.

Resuming the previously discussed results, low errors are observed in the case of diffusion expected to be approximately Gaussian; extracellular compartment diffusion in this case. Strongly restricted intracellular diffusion is poorly represented because its highly non-Gaussian. In the case of a single complete bundle, simple Zeppelin consistently underestimates orthogonal diffusion, and the deviation worsens when the volume fraction of the substrate increases. The histogram experiments might help understanding why this happens, as the non Gaussianity of the intracellular part of the diffusion tends to dominate when f increases. When f is known beforehand, the zeppelin + stick model improves quality substantially. The deviation also increases proportional to f, but in a quite less steep fashion. The estimation error is almost the same for all used rotation angles of the crossings, so low variability mean it might be possible to compensate for it. Finally, in the more realistic experiment of 4 degrees of freedom search, the problem is impossible to solve when the acquisition protocol is limited to one b-value. Nevertheless, in the 1 shell experiment, the angle θ and mix factor α are correctly inferred. When 4 shells are used, the results are of very high quality, surpassing even the one bundle results. There is no worsening trend in the predictions of the orthogonal coefficient $D_{\parallel}$ or f. We speculate this is caused by effects of another bundle with the exact same characteristics.

6.1 Limitations

We limited the scope of this work to widely used bi-compartment models with a low count of parameters in order to do a local exhaustive search. However, there is evidence that 3 compartments or more, plus the addition of isotropically restricted models, attain better results for real data, at the expense of increasing model complexity (Panagiotaki et al., 2012). By the intrinsic nature of the models used (statistical models that describe

the averaged ensemble characteristics), we focused only in recovering apparent diffusion coefficients, volume fraction and crossing angles (one of them). There are various biophysical, statistical and models proposed to associate patterns in the acquired signal to microstructural features, such as axon diameter and fiber density (Daducci, Erick Jorge Canales-Rodríguez, et al., 2013) (Daducci, Erick J Canales-Rodríguez, et al., 2015). One difference between some of them and DTI based models is they require a specific measuring scheme with a specific set of directions and shells (Jelescu and Budde, 2017). In terms of our framework, comparison is possible as one would only need to repeat the signal acquisition step with the same synthetic data.

6.2 Future Work

We could not characterize the search space near the ground truth neighborhood, along all the possible degrees of freedom, because of time constraints. Another immediate followup is to augment the substrate complexity. It is possible to simulate the diffusion process on arbitrary 3D meshes, which can be modelled based on real electron microscopy observation of axons with rich geometrical features, undulations and so forth. It would be interesting to create various types of realistic substrates based on different regions of the brain to assess if the modelling error could depend on the place where the signal was retrieved. We might also adapt the methodology to characterize the error of the more sophisticated biophysical presented discussed in the former section. Study the effects of multiple unknown number of crossing fibers on the fitting could be interesting, as we could fit iteratively an increasing number of models (Zhu et al., 2013). A kind of binary search could be done to decrease the time complexity on the intuition that the nearer the number of models to the real number of crossing fibers, the better the used distance metrics are.

Appendix A

Details Of The Used MRI Protocols

A.1 Directions used in each shell

	g_x	g_y	g_z		g_x	g_y	g_z		g_x	g_y	g_z
1	0.8764	-0.1992	0.4385	31	0.1489	0.2300	0.9617	61	0.9977	-0.0401	-0.0546
2	0.2555	-0.0611	0.9649	32	-0.1683	0.9780	0.1232	62	0.2694	0.9270	0.2610
3	0.1437	-0.2180	-0.9653	33	-0.2740	0.4232	0.8636	63	0.4888	-0.2728	-0.8286
4	-0.1045	-0.9930	-0.0543	34	-0.7120	0.1554	-0.6847	64	-0.2558	0.9044	-0.3416
5	0.1661	0.8334	0.5271	35	0.9617	-0.2468	0.1194	65	-0.4751	-0.4502	0.7561
6	-0.1898	-0.9454	0.2649	36	0.0537	-0.9854	0.1614	66	0.3421	0.6470	0.6814
7	-0.9580	-0.1768	0.2258	37	0.4046	0.1656	0.8994	67	-0.6850	-0.2197	0.6946
8	0.0147	-0.8923	0.4512	38	-0.3969	0.7317	0.5541	68	0.8579	-0.4226	0.2924
9	-0.0167	0.7328	-0.6803	39	-0.7354	-0.3011	-0.6071	69	0.4605	-0.8762	-0.1424
10	-0.6404	-0.6879	-0.3416	40	0.8756	-0.4829	-0.0080	70	-0.9126	-0.3990	0.0887
11	0.5072	0.8471	0.1586	41	0.9048	0.2331	0.3565	71	-0.2148	-0.1504	0.9650
12	0.0000	0.0000	1.0000	42	0.7475	-0.6453	0.1578	72	0.4853	-0.7836	0.3878
13	0.7739	0.6134	-0.1578	43	-0.1120	0.8232	0.5566	73	0.4202	0.7878	0.4503
14	-0.6163	0.0309	0.7869	44	0.8377	0.0492	0.5439	74	0.2668	-0.7681	0.5821
15	0.2732	-0.5706	0.7744	45	-0.4818	0.5252	0.7015	75	0.0763	0.6728	0.7359
16	-0.9652	0.0183	-0.2607	46	0.6925	-0.7138	-0.1046	76	0.7221	-0.3972	0.5664
17	0.8528	0.1893	-0.4868	47	-0.6893	0.3032	0.6580	77	0.2919	-0.3321	0.8970
18	0.0377	-0.2773	0.9601	48	0.8754	0.4539	0.1663	78	-0.8438	0.3110	0.4374
19	-0.3470	-0.9367	0.0470	49	0.6799	-0.6075	0.4107	79	-0.4988	0.6057	-0.6199
20	0.0208	-0.5218	0.8528	50	-0.4628	-0.6678	0.5830	80	0.2720	0.4502	0.8505
21	-0.0010	0.4615	0.8871	51	-0.6679	0.5420	0.5100	81	-0.5803	-0.8063	0.1146
22	0.2936	-0.8873	-0.3556	52	-0.2015	0.6447	0.7374	82	0.3234	-0.9421	0.0887
23	0.9356	-0.0624	-0.3476	53	0.8019	-0.5316	-0.2728	83	-0.2323	-0.4026	0.8854
24	0.5790	0.5645	0.5884	54	0.6429	0.6636	-0.3826	84	0.7339	0.6725	0.0958
25	-0.9424	0.2840	0.1769	55	-0.5543	0.8221	-0.1297	85	0.9778	0.1923	0.0833
26	-0.5745	0.7387	0.3525	56	-0.0004	-0.9438	-0.3305	86	-0.6777	-0.4597	0.5739
27	0.4970	-0.1175	0.8597	57	-0.4664	-0.2006	0.8615	87	-0.2307	-0.8152	0.5312
28	0.6388	0.1032	0.7624	58	-0.4294	-0.8377	0.3375	88	0.8321	0.4232	-0.3585
29	0.7791	0.4736	0.4107	59	0.5250	-0.3770	0.7631	89	-0.3628	0.0647	0.9296
30	-0.8035	0.0570	0.5926	60	0.5172	0.3766	0.7686	90	-0.2348	-0.6297	0.7406

A.2 Complete protocol

The two used protocols in CAMINO textfile format can be downloaded.

1-shell protocol: https://gitlab.com/ponco0e/tesis-cimat/blob/56a0949bc0bfe3cab5c8a87730023776e
recorrersimuladormc/schemes/moddedDyrby_1shell_b1000.0.txt

4 shell protocol: https://gitlab.com/ponco0e/tesis-cimat/blob/56a0949bc0bfe3cab5c8a87730023recorrersimuladormc/schemes/moddedDyrby_3shell.txt.

Appendix B

Complete Experimental Results

TABLE B.1: Complete Results of MRI Model Fitting Experiment. The table shows the relative error between the predicted $D_\perp$ for each bundle and the respective ground truth.

	bundle			bundleStick			extra			intra		
Label	$\hat{D}_\perp$	$D_\perp$	$\varepsilon(\hat{D}_\perp)$	$\hat{D}_\perp$	$D_\perp$	$\varepsilon(\hat{D}_\perp)$	$\hat{D}_\perp$	$D_\perp$	$\varepsilon(\hat{D}_\perp)$	$\hat{D}_\perp$	$D_\perp$	$\varepsilon(\hat{D}_\perp)$
lvl2	1.034140e-09	1.336526e-09	-22.62%	1.587379e-09	1.675833e-09	-5.28%	1.594544e-09	1.675833e-09	-4.85%	3.093961e-15	3.093961e-12	-99.90%
lvl3	7.583010e-10	1.025719e-09	-26.07%	1.404051e-09	1.481336e-09	-5.22%	1.409023e-09	1.481336e-09	-4.88%	2.646827e-15	2.646827e-12	-99.90%
lvl4	5.776136e-10	7.998587e-10	-27.79%	1.256263e-09	1.334570e-09	-5.87%	1.266288e-09	1.334570e-09	-5.12%	2.605884e-15	2.605884e-12	-99.90%
lvl5	4.127837e-10	5.801882e-10	-28.85%	1.094264e-09	1.161685e-09	-5.80%	1.104268e-09	1.161685e-09	-4.94%	2.464086e-15	2.464086e-12	-99.90%
lvl6	2.769669e-10	3.912025e-10	-29.20%	9.305449e-10	9.930067e-10	-6.29%	9.417050e-10	9.930067e-10	-5.17%	2.558570e-15	2.558570e-12	-99.90%
lvl7	1.701321e-10	2.350369e-10	-27.61%	7.395612e-10	7.948297e-10	-6.95%	7.547828e-10	7.948297e-10	-5.04%	2.432815e-15	2.432815e-12	-99.90%

TABLE B.2: Complete results of 3DOF search fitting $\theta, D_\parallel, D_\perp$ using Zeppelin. The table shows the relative error between the predicted parameters for each bundle and the respective ground truth.

Level	$D_\parallel$	$D_\perp$	θ	α	$\hat{D}_\parallel$	$\hat{D}_\perp$	$\hat{\theta}$	$\varepsilon(\hat{D}_\parallel)$	$\varepsilon(\hat{D}_\perp)$	$\varepsilon(\hat{\theta})$
lvl2	2.100000e-09	1.336526e-09	60.0	0.5	2.141958e-09	1.016080e-09	61.1988	2.00%	-23.98%	2.00%
	2.100000e-09	1.336526e-09	70.0	0.5	2.183916e-09	1.016080e-09	71.3986	4.00%	-23.98%	2.00%
	2.100000e-09	1.336526e-09	80.0	0.5	2.183916e-09	1.016080e-09	81.5984	4.00%	-23.98%	2.00%
	2.100000e-09	1.336526e-09	90.0	0.5	2.183916e-09	1.016080e-09	90.0000	4.00%	-23.98%	0.00%
lvl3	2.100000e-09	1.025719e-09	60.0	0.5	2.100000e-09	7.592987e-10	60.0000	0.00%	-25.97%	-0.00%
	2.100000e-09	1.025719e-09	70.0	0.5	2.100000e-09	7.592987e-10	70.0000	0.00%	-25.97%	0.00%
	2.100000e-09	1.025719e-09	80.0	0.5	2.100000e-09	7.592987e-10	80.0000	0.00%	-25.97%	0.00%
	2.100000e-09	1.025719e-09	90.0	0.5	2.100000e-09	7.592987e-10	90.0000	0.00%	-25.97%	0.00%
lvl4	2.100000e-09	7.998587e-10	60.0	0.5	2.100000e-09	5.761222e-10	60.0000	0.00%	-27.97%	-0.00%
	2.100000e-09	7.998587e-10	70.0	0.5	2.100000e-09	5.761222e-10	70.0000	0.00%	-27.97%	0.00%
	2.100000e-09	7.998587e-10	80.0	0.5	2.100000e-09	5.761222e-10	80.0000	0.00%	-27.97%	0.00%
	2.100000e-09	7.998587e-10	90.0	0.5	2.100000e-09	5.761222e-10	90.0000	0.00%	-27.97%	0.00%
lvl5	2.100000e-09	5.801882e-10	60.0	0.5	2.058042e-09	4.178980e-10	60.0000	-2.00%	-27.97%	-0.00%
	2.100000e-09	5.801882e-10	70.0	0.5	2.058042e-09	4.178980e-10	70.0000	-2.00%	-27.97%	0.00%
	2.100000e-09	5.801882e-10	80.0	0.5	2.058042e-09	4.178980e-10	80.0000	-2.00%	-27.97%	0.00%
	2.100000e-09	5.801882e-10	90.0	0.5	2.100000e-09	4.063058e-10	90.0000	0.00%	-29.97%	0.00%
lvl6	2.100000e-09	3.912025e-10	60.0	0.5	2.058042e-09	2.817753e-10	60.0000	-2.00%	-27.97%	-0.00%
	2.100000e-09	3.912025e-10	70.0	0.5	2.058042e-09	2.817753e-10	70.0000	-2.00%	-27.97%	0.00%
	2.100000e-09	3.912025e-10	80.0	0.5	2.100000e-09	2.739591e-10	80.0000	0.00%	-29.97%	0.00%
	2.100000e-09	3.912025e-10	90.0	0.5	2.100000e-09	2.739591e-10	90.0000	0.00%	-29.97%	0.00%
lvl7	2.100000e-09	2.350369e-10	60.0	0.5	2.058042e-09	1.739884e-10	60.0000	-2.00%	-25.97%	-0.00%
	2.100000e-09	2.350369e-10	70.0	0.5	2.058042e-09	1.739884e-10	70.0000	-2.00%	-25.97%	0.00%
	2.100000e-09	2.350369e-10	80.0	0.5	2.058042e-09	1.692924e-10	80.0000	-2.00%	-27.97%	0.00%
	2.100000e-09	2.350369e-10	90.0	0.5	2.058042e-09	1.692924e-10	90.0000	-2.00%	-27.97%	0.00%

TABLE B.3: Complete results of 3DOF search fitting $\theta, D_{\parallel}, D_{\perp}$ using Zeppelin-Stick. The table shows the relative error between the predicted parameters for each bundle and the respective ground truth.

Level	$D_{\parallel}$	$D_{\perp}$	θ	α	$\hat{D}_{\parallel}$	$\hat{D}_{\perp}$	$\hat{\theta}$	$\varepsilon(\hat{D}_{\parallel})$	$\varepsilon(\hat{D}_{\perp})$	$\varepsilon(\hat{\theta})$
lvl2	2.100000e-09	1.675833e-09	60.0	0.5	2.016084e-09	1.608866e-09	60.0	-4.00%	-4.00%	-0.00%
	2.100000e-09	1.675833e-09	70.0	0.5	2.016084e-09	1.608866e-09	70.0	-4.00%	-4.00%	0.00%
	2.100000e-09	1.675833e-09	80.0	0.5	2.016084e-09	1.608866e-09	80.0	-4.00%	-4.00%	0.00%
	2.100000e-09	1.675833e-09	90.0	0.5	2.016084e-09	1.608866e-09	90.0	-4.00%	-4.00%	0.00%
lvl3	2.100000e-09	1.481336e-09	60.0	0.5	2.016084e-09	1.422142e-09	60.0	-4.00%	-4.00%	-0.00%
	2.100000e-09	1.481336e-09	70.0	0.5	2.016084e-09	1.422142e-09	70.0	-4.00%	-4.00%	0.00%
	2.100000e-09	1.481336e-09	80.0	0.5	2.016084e-09	1.422142e-09	80.0	-4.00%	-4.00%	0.00%
	2.100000e-09	1.481336e-09	90.0	0.5	2.016084e-09	1.422142e-09	90.0	-4.00%	-4.00%	0.00%
lvl4	2.100000e-09	1.334570e-09	60.0	0.5	2.016084e-09	1.307905e-09	60.0	-4.00%	-2.00%	-0.00%
	2.100000e-09	1.334570e-09	70.0	0.5	2.016084e-09	1.307905e-09	70.0	-4.00%	-2.00%	0.00%
	2.100000e-09	1.334570e-09	80.0	0.5	2.016084e-09	1.307905e-09	80.0	-4.00%	-2.00%	0.00%
	2.100000e-09	1.334570e-09	90.0	0.5	2.016084e-09	1.307905e-09	90.0	-4.00%	-2.00%	0.00%
lvl5	2.100000e-09	1.161685e-09	60.0	0.5	2.016084e-09	1.138474e-09	60.0	-4.00%	-2.00%	-0.00%
	2.100000e-09	1.161685e-09	70.0	0.5	2.016084e-09	1.138474e-09	70.0	-4.00%	-2.00%	0.00%
	2.100000e-09	1.161685e-09	80.0	0.5	2.016084e-09	1.138474e-09	80.0	-4.00%	-2.00%	0.00%
	2.100000e-09	1.161685e-09	90.0	0.5	2.016084e-09	1.138474e-09	90.0	-4.00%	-2.00%	0.00%
lvl6	2.100000e-09	9.930067e-10	60.0	0.5	2.016084e-09	9.731665e-10	60.0	-4.00%	-2.00%	-0.00%
	2.100000e-09	9.930067e-10	70.0	0.5	2.016084e-09	9.731665e-10	70.0	-4.00%	-2.00%	0.00%
	2.100000e-09	9.930067e-10	80.0	0.5	2.058042e-09	9.334859e-10	80.0	-2.00%	-5.99%	0.00%
	2.100000e-09	9.930067e-10	90.0	0.5	2.058042e-09	9.334859e-10	90.0	-2.00%	-5.99%	0.00%
lvl7	2.100000e-09	7.948297e-10	60.0	0.5	2.016084e-09	7.948297e-10	60.0	-4.00%	0.00%	-0.00%
	2.100000e-09	7.948297e-10	70.0	0.5	2.016084e-09	7.789490e-10	70.0	-4.00%	-2.00%	0.00%
	2.100000e-09	7.948297e-10	80.0	0.5	2.016084e-09	7.789490e-10	80.0	-4.00%	-2.00%	0.00%
	2.100000e-09	7.948297e-10	90.0	0.5	2.016084e-09	7.789490e-10	90.0	-4.00%	-2.00%	0.00%

TABLE B.4: Complete results of 3DOF search fitting $\alpha, D_{\parallel}, D_{\perp}$ using Zeppelin. The table shows the relative error between the predicted parameters for each bundle and the respective ground truth.

Level	$D_{\parallel}$	$D_{\perp}$	θ	α	$\hat{D}_{\parallel}$	$\hat{D}_{\perp}$	$\hat{\alpha}$	$\varepsilon(\hat{D}_{\parallel})$	$\varepsilon(\hat{D}_{\perp})$	$\varepsilon(\hat{\alpha})$
lvl2	2.100000e-09	1.336526e-09	60.0	0.5	2.141958e-09	1.016080e-09	0.5	2.00%	-23.98%	0.00%
	2.100000e-09	1.336526e-09	70.0	0.5	2.141958e-09	1.016080e-09	0.5	2.00%	-23.98%	0.00%
	2.100000e-09	1.336526e-09	80.0	0.5	2.183916e-09	1.016080e-09	0.5	4.00%	-23.98%	0.00%
	2.100000e-09	1.336526e-09	90.0	0.5	2.183916e-09	1.016080e-09	0.5	4.00%	-23.98%	0.00%
lvl3	2.100000e-09	1.025719e-09	60.0	0.5	2.100000e-09	7.592987e-10	0.5	0.00%	-25.97%	0.00%
	2.100000e-09	1.025719e-09	70.0	0.5	2.100000e-09	7.592987e-10	0.5	0.00%	-25.97%	0.00%
	2.100000e-09	1.025719e-09	80.0	0.5	2.100000e-09	7.592987e-10	0.5	0.00%	-25.97%	0.00%
	2.100000e-09	1.025719e-09	90.0	0.5	2.100000e-09	7.592987e-10	0.5	0.00%	-25.97%	0.00%
lvl4	2.100000e-09	7.998587e-10	60.0	0.5	2.100000e-09	5.761222e-10	0.5	0.00%	-27.97%	0.00%
	2.100000e-09	7.998587e-10	70.0	0.5	2.100000e-09	5.761222e-10	0.5	0.00%	-27.97%	0.00%
	2.100000e-09	7.998587e-10	80.0	0.5	2.100000e-09	5.761222e-10	0.5	0.00%	-27.97%	0.00%
	2.100000e-09	7.998587e-10	90.0	0.5	2.100000e-09	5.761222e-10	0.5	0.00%	-27.97%	0.00%
lvl5	2.100000e-09	5.801882e-10	60.0	0.5	2.058042e-09	4.178980e-10	0.5	-2.00%	-27.97%	0.00%
	2.100000e-09	5.801882e-10	70.0	0.5	2.058042e-09	4.178980e-10	0.5	-2.00%	-27.97%	0.00%
	2.100000e-09	5.801882e-10	80.0	0.5	2.058042e-09	4.178980e-10	0.5	-2.00%	-27.97%	0.00%
	2.100000e-09	5.801882e-10	90.0	0.5	2.100000e-09	4.063058e-10	0.5	0.00%	-29.97%	0.00%
lvl6	2.100000e-09	3.912025e-10	60.0	0.5	2.058042e-09	2.817753e-10	0.5	-2.00%	-27.97%	0.00%
	2.100000e-09	3.912025e-10	70.0	0.5	2.058042e-09	2.817753e-10	0.5	-2.00%	-27.97%	0.00%
	2.100000e-09	3.912025e-10	80.0	0.5	2.100000e-09	2.739591e-10	0.5	0.00%	-29.97%	0.00%
	2.100000e-09	3.912025e-10	90.0	0.5	2.100000e-09	2.739591e-10	0.5	0.00%	-29.97%	0.00%
lvl7	2.100000e-09	2.350369e-10	60.0	0.5	2.058042e-09	1.739884e-10	0.5	-2.00%	-25.97%	0.00%
	2.100000e-09	2.350369e-10	70.0	0.5	2.058042e-09	1.739884e-10	0.5	-2.00%	-25.97%	0.00%
	2.100000e-09	2.350369e-10	80.0	0.5	2.058042e-09	1.692924e-10	0.5	-2.00%	-27.97%	0.00%
	2.100000e-09	2.350369e-10	90.0	0.5	2.058042e-09	1.692924e-10	0.5	-2.00%	-27.97%	0.00%

TABLE B.5: Complete results of 3DOF search fitting $\alpha, D_{\parallel}, D_{\perp}$ using Zeppelin-Stick. The table shows the relative error between the predicted parameters for each bundle and the respective ground truth.

Level	$D_{\parallel}$	$D_{\perp}$	θ	α	$\hat{D}_{\parallel}$	$\hat{D}_{\perp}$	$\hat{\alpha}$	$\varepsilon(\hat{D}_{\parallel})$	$\varepsilon(\hat{D}_{\perp})$	$\varepsilon(\hat{\alpha})$
lvl2	2.100000e-09	1.675833e-09	60.0	0.5	2.016084e-09	1.608866e-09	0.5	-4.00%	-4.00%	0.00%
	2.100000e-09	1.675833e-09	70.0	0.5	2.016084e-09	1.608866e-09	0.5	-4.00%	-4.00%	0.00%
	2.100000e-09	1.675833e-09	80.0	0.5	2.016084e-09	1.608866e-09	0.5	-4.00%	-4.00%	0.00%
	2.100000e-09	1.675833e-09	90.0	0.5	2.016084e-09	1.608866e-09	0.5	-4.00%	-4.00%	0.00%
lvl3	2.100000e-09	1.481336e-09	60.0	0.5	2.016084e-09	1.422142e-09	0.5	-4.00%	-4.00%	0.00%
	2.100000e-09	1.481336e-09	70.0	0.5	2.016084e-09	1.422142e-09	0.5	-4.00%	-4.00%	0.00%
	2.100000e-09	1.481336e-09	80.0	0.5	2.016084e-09	1.422142e-09	0.5	-4.00%	-4.00%	0.00%
	2.100000e-09	1.481336e-09	90.0	0.5	2.016084e-09	1.422142e-09	0.5	-4.00%	-4.00%	0.00%
lvl4	2.100000e-09	1.334570e-09	60.0	0.5	2.016084e-09	1.307905e-09	0.5	-4.00%	-2.00%	0.00%
	2.100000e-09	1.334570e-09	70.0	0.5	2.016084e-09	1.307905e-09	0.5	-4.00%	-2.00%	0.00%
	2.100000e-09	1.334570e-09	80.0	0.5	2.016084e-09	1.307905e-09	0.5	-4.00%	-2.00%	0.00%
	2.100000e-09	1.334570e-09	90.0	0.5	2.016084e-09	1.307905e-09	0.5	-4.00%	-2.00%	0.00%
lvl5	2.100000e-09	1.161685e-09	60.0	0.5	2.016084e-09	1.138474e-09	0.5	-4.00%	-2.00%	0.00%
	2.100000e-09	1.161685e-09	70.0	0.5	2.016084e-09	1.138474e-09	0.5	-4.00%	-2.00%	0.00%
	2.100000e-09	1.161685e-09	80.0	0.5	2.016084e-09	1.138474e-09	0.5	-4.00%	-2.00%	0.00%
	2.100000e-09	1.161685e-09	90.0	0.5	2.016084e-09	1.138474e-09	0.5	-4.00%	-2.00%	0.00%
lvl6	2.100000e-09	9.930067e-10	60.0	0.5	2.016084e-09	9.731665e-10	0.5	-4.00%	-2.00%	0.00%
	2.100000e-09	9.930067e-10	70.0	0.5	2.016084e-09	9.731665e-10	0.5	-4.00%	-2.00%	0.00%
	2.100000e-09	9.930067e-10	80.0	0.5	2.058042e-09	9.334859e-10	0.5	-2.00%	-5.99%	0.00%
	2.100000e-09	9.930067e-10	90.0	0.5	2.058042e-09	9.334859e-10	0.5	-2.00%	-5.99%	0.00%
lvl7	2.100000e-09	7.948297e-10	60.0	0.5	2.016084e-09	7.948297e-10	0.5	-4.00%	0.00%	0.00%
	2.100000e-09	7.948297e-10	70.0	0.5	2.016084e-09	7.789490e-10	0.5	-4.00%	-2.00%	0.00%
	2.100000e-09	7.948297e-10	80.0	0.5	2.016084e-09	7.789490e-10	0.5	-4.00%	-2.00%	0.00%
	2.100000e-09	7.948297e-10	90.0	0.5	2.016084e-09	7.789490e-10	0.5	-4.00%	-2.00%	0.00%

TABLE B.6: Complete results of 4DOF search using Zeppelin + Stick with one shell. The table shows the relative error between the predicted parameters for each bundle and the respective ground truth.

Label	$D_\perp$	f	θ	α	$\hat{D}_\perp$	$\hat{\alpha}$	$\hat{\theta}$	$\hat{f}$	$\varepsilon(\hat{\theta})$	$\varepsilon(\hat{D}_\perp)$	$\varepsilon(\hat{f})$	$\varepsilon(\hat{\alpha})$
lvl2	1.675833e-09	0.202845	60.0	0.5	1.341001e-09	0.51998	62.3976	0.138000	4.00%	-19.98%	-31.97%	4.00%
	1.675833e-09	0.202845	70.0	0.5	1.341001e-09	0.50000	70.0000	0.138000	0.00%	-19.98%	-31.97%	0.00%
	1.675833e-09	0.202845	80.0	0.5	1.341001e-09	0.50000	80.0000	0.138000	0.00%	-19.98%	-31.97%	0.00%
	1.675833e-09	0.202845	90.0	0.5	1.341001e-09	0.50000	90.0000	0.138000	0.00%	-19.98%	-31.97%	0.00%
lvl3	1.481336e-09	0.308122	60.0	0.5	1.066977e-09	0.50000	60.0000	0.197309	-0.00%	-27.97%	-35.96%	0.00%
	1.481336e-09	0.308122	70.0	0.5	1.066977e-09	0.50000	70.0000	0.197309	0.00%	-27.97%	-35.96%	0.00%
	1.481336e-09	0.308122	80.0	0.5	1.066977e-09	0.50000	80.0000	0.197309	0.00%	-27.97%	-35.96%	0.00%
	1.481336e-09	0.308122	90.0	0.5	1.066977e-09	0.50000	90.0000	0.197309	0.00%	-27.97%	-35.96%	0.00%
lvl4	1.334570e-09	0.401446	60.0	0.5	6.946169e-10	0.50000	60.0000	0.128736	-0.00%	-47.95%	-67.93%	0.00%
	1.334570e-09	0.401446	70.0	0.5	6.946169e-10	0.50000	70.0000	0.128736	0.00%	-47.95%	-67.93%	0.00%
	1.334570e-09	0.401446	80.0	0.5	6.946169e-10	0.50000	80.0000	0.128736	0.00%	-47.95%	-67.93%	0.00%
	1.334570e-09	0.401446	90.0	0.5	6.946169e-10	0.50000	90.0000	0.128736	0.00%	-47.95%	-67.93%	0.00%
lvl5	1.161685e-09	0.501627	60.0	0.5	5.117918e-10	0.50000	60.0000	0.160862	-0.00%	-55.94%	-67.93%	0.00%
	1.161685e-09	0.501627	70.0	0.5	5.117918e-10	0.50000	70.0000	0.160862	0.00%	-55.94%	-67.93%	0.00%
	1.161685e-09	0.501627	80.0	0.5	5.117918e-10	0.50000	80.0000	0.160862	0.00%	-55.94%	-67.93%	0.00%
	1.161685e-09	0.501627	90.0	0.5	5.117918e-10	0.50000	90.0000	0.160862	0.00%	-55.94%	-67.93%	0.00%
lvl6	9.930067e-10	0.607608	60.0	0.5	3.184374e-10	0.50000	60.0000	0.122008	-0.00%	-67.93%	-79.92%	0.00%
	9.930067e-10	0.607608	70.0	0.5	2.787568e-10	0.50000	70.0000	0.024888	0.00%	-71.93%	-95.90%	0.00%
	9.930067e-10	0.607608	80.0	0.5	2.787568e-10	0.50000	80.0000	0.024888	0.00%	-71.93%	-95.90%	0.00%
	9.930067e-10	0.607608	90.0	0.5	2.787568e-10	0.50000	90.0000	0.024888	0.00%	-71.93%	-95.90%	0.00%
lvl7	7.948297e-10	0.706455	60.0	0.5	1.913632e-10	0.50000	60.0000	0.141856	-0.00%	-75.92%	-79.92%	0.00%
	7.948297e-10	0.706455	70.0	0.5	1.913632e-10	0.50000	70.0000	0.141856	0.00%	-75.92%	-79.92%	0.00%
	7.948297e-10	0.706455	80.0	0.5	1.913632e-10	0.50000	80.0000	0.141856	0.00%	-75.92%	-79.92%	0.00%
	7.948297e-10	0.706455	90.0	0.5	1.913632e-10	0.50000	90.0000	0.141856	0.00%	-75.92%	-79.92%	0.00%

TABLE B.7: Complete results of 4DOF search using Zeppelin + Stick with four shells. The table shows the relative error between the predicted parameters for each bundle and the respective ground truth.

Label	$D_\perp$	f	θ	α	$\hat{D}_\perp$	$\hat{\alpha}$	$\hat{\theta}$	$\hat{f}$	$\varepsilon(\hat{\theta})$	$\varepsilon(\hat{D}_\perp)$	$\varepsilon(\hat{f})$	$\varepsilon(\hat{\alpha})$
lvl2	1.675833e-09	0.202845	60.0	0.5	1.608866e-09	0.5	60.0	0.210951	-0.00%	-4.00%	4.00%	0.00%
	1.675833e-09	0.202845	70.0	0.5	1.541900e-09	0.5	70.0	0.202845	0.00%	-7.99%	-0.00%	0.00%
	1.675833e-09	0.202845	80.0	0.5	1.541900e-09	0.5	80.0	0.202845	0.00%	-7.99%	-0.00%	0.00%
	1.675833e-09	0.202845	90.0	0.5	1.541900e-09	0.5	90.0	0.202845	0.00%	-7.99%	-0.00%	0.00%
lvl3	1.481336e-09	0.308122	60.0	0.5	1.362948e-09	0.5	60.0	0.308122	-0.00%	-7.99%	0.00%	0.00%
	1.481336e-09	0.308122	70.0	0.5	1.362948e-09	0.5	70.0	0.308122	0.00%	-7.99%	0.00%	0.00%
	1.481336e-09	0.308122	80.0	0.5	1.362948e-09	0.5	80.0	0.308122	0.00%	-7.99%	0.00%	0.00%
	1.481336e-09	0.308122	90.0	0.5	1.362948e-09	0.5	90.0	0.308122	0.00%	-7.99%	0.00%	0.00%
lvl4	1.334570e-09	0.401446	60.0	0.5	1.227911e-09	0.5	60.0	0.401446	-0.00%	-7.99%	0.00%	0.00%
	1.334570e-09	0.401446	70.0	0.5	1.227911e-09	0.5	70.0	0.401446	0.00%	-7.99%	0.00%	0.00%
	1.334570e-09	0.401446	80.0	0.5	1.227911e-09	0.5	80.0	0.401446	0.00%	-7.99%	0.00%	0.00%
	1.334570e-09	0.401446	90.0	0.5	1.227911e-09	0.5	90.0	0.401446	0.00%	-7.99%	0.00%	0.00%
lvl5	1.161685e-09	0.501627	60.0	0.5	1.068843e-09	0.5	60.0	0.501627	-0.00%	-7.99%	0.00%	0.00%
	1.161685e-09	0.501627	70.0	0.5	1.068843e-09	0.5	70.0	0.501627	0.00%	-7.99%	0.00%	0.00%
	1.161685e-09	0.501627	80.0	0.5	1.068843e-09	0.5	80.0	0.501627	0.00%	-7.99%	0.00%	0.00%
	1.161685e-09	0.501627	90.0	0.5	1.068843e-09	0.5	90.0	0.501627	0.00%	-7.99%	0.00%	0.00%
lvl6	9.930067e-10	0.607608	60.0	0.5	9.136456e-10	0.5	60.0	0.607608	-0.00%	-7.99%	0.00%	0.00%
	9.930067e-10	0.607608	70.0	0.5	8.739651e-10	0.5	70.0	0.607608	0.00%	-11.99%	0.00%	0.00%
	9.930067e-10	0.607608	80.0	0.5	8.739651e-10	0.5	80.0	0.607608	0.00%	-11.99%	0.00%	0.00%
	9.930067e-10	0.607608	90.0	0.5	8.739651e-10	0.5	90.0	0.607608	0.00%	-11.99%	0.00%	0.00%
lvl7	7.948297e-10	0.706455	60.0	0.5	6.995455e-10	0.5	60.0	0.706455	-0.00%	-11.99%	0.00%	0.00%
	7.948297e-10	0.706455	70.0	0.5	6.995455e-10	0.5	70.0	0.706455	0.00%	-11.99%	0.00%	0.00%
	7.948297e-10	0.706455	80.0	0.5	6.995455e-10	0.5	80.0	0.706455	0.00%	-11.99%	0.00%	0.00%
	7.948297e-10	0.706455	90.0	0.5	6.995455e-10	0.5	90.0	0.706455	0.00%	-11.99%	0.00%	0.00%

Bibliography

Aboitiz, Francisco et al. (1992). "Fiber composition of the human corpus callosum". In: *Brain research* 598.1-2, pp. 143–153.

Abragam, Anatole (1961). *The principles of nuclear magnetism*. 32. Oxford university press.

Alexander, Daniel C (2008). "A general framework for experiment design in diffusion MRI and its application in measuring direct tissue-microstructure features". In: *Magnetic Resonance in Medicine: An Official Journal of the International Society for Magnetic Resonance in Medicine* 60.2, pp. 439–448.

Alexander, Daniel C and Kiran K Seunarine (2010). "Mathematics of crossing fibers". In: *Diffusion MRI: theory, methods, and applications*. Oxford University Press, pp. 451–464.

Aragones, Enriqueta et al. (2002). "Accuracy vs. simplicity: A complex trade-off". In:

Assaf, Yaniv et al. (2008). "AxCaliber: a method for measuring axon diameter distribution from diffusion MRI". In: *Magnetic Resonance in Medicine: An Official Journal of the International Society for Magnetic Resonance in Medicine* 59.6, pp. 1347–1354.

Aung, Wint Yan, Soe Mar, and Tammie LS Benzinger (2013). "Diffusion tensor MRI as a biomarker in axonal and myelin damage". In: *Imaging in medicine* 5.5, p. 427.

Back, Stephen A et al. (2011). "White matter lesions defined by diffusion tensor imaging in older adults". In: *Annals of neurology* 70.3, pp. 465–476.

Bar-Shir, Amnon, Ian D Duncan, and Yoram Cohen (2009). "QSI and DTI of excised brains of the myelin-deficient rat". In: *Neuroimage* 48.1, pp. 109–116.

Basser, Peter J (2002). "Relationships between diffusion tensor and q-space MRI". In: *Magnetic Resonance in Medicine: An Official Journal of the International Society for Magnetic Resonance in Medicine* 47.2, pp. 392–397.

Basser, Peter J, James Mattiello, and Denis LeBihan (1994). "Estimation of the effective self-diffusion tensor from the NMR spin echo". In: *Journal of Magnetic Resonance, Series B* 103.3, pp. 247–254.

Basser, Peter J and Sinisa Pajevic (2000). "Statistical artifacts in diffusion tensor MRI (DT-MRI) caused by background noise". In: *Magnetic Resonance in Medicine: An Official Journal of the International Society for Magnetic Resonance in Medicine* 44.1, pp. 41–50.

Basser, Peter J and Carlo Pierpaoli (1996). "Microstructural and physiological features of tissues elucidated by quantitative-diffusion-tensor MRI". In: *Journal of Magnetic Resonance - Series B* 111.3, pp. 209–219. ISSN: 10641866. DOI: 10.1006/jmrb.1996.0086. URL: http://www.sciencedirect.com/science/article/pii/S109078071100334X.

Beaulieu, Christian (2002). "The basis of anisotropic water diffusion in the nervous system–a technical review". In: *NMR in Biomedicine: An International Journal Devoted to the Development and Application of Magnetic Resonance In Vivo* 15.7-8, pp. 435–455.

— (2014). "The biological basis of diffusion anisotropy". In: *Diffusion MRI:Diffusion MRI: from quantitative measurement to in vivo neuroanatomy*. Elsevier, pp. 155–183.

Beaulieu, Christian and Peter S Allen (1994a). "Determinants of anisotropic water diffusion in nerves". In: *Magnetic resonance in medicine* 31.4, pp. 394–400.

Beaulieu, Christian and Peter S Allen (1994b). "Water diffusion in the giant axon of the squid: implications for diffusion-weighted MRI of the nervous system". In: *Magnetic Resonance in Medicine* 32.5, pp. 579–583.

Behrens, Timothy EJ et al. (2003). "Characterization and propagation of uncertainty in diffusion-weighted MR imaging". In: *Magnetic Resonance in Medicine: An Official Journal of the International Society for Magnetic Resonance in Medicine* 50.5, pp. 1077–1088.

Bloembergen, Nicolaas, Edward Mills Purcell, and Robert V Pound (1948). "Relaxation effects in nuclear magnetic resonance absorption". In: *Physical review* 73.7, p. 679.

Bouchaud, Jean-Philippe and Antoine Georges (1990). "Anomalous diffusion in disordered media: statistical mechanisms, models and physical applications". In: *Physics reports* 195.4-5, pp. 127–293.

Brangwynne, Clifford P. et al. (2008). *Cytoplasmic diffusion: Molecular motors mix it up*. DOI: 10.1083/jcb.200806149. URL: www.jcb.org/cgi/doi/10.1083/jcb.200806149.

Brown, Robert (1828). "XXVII. A brief account of microscopical observations made in the months of June, July and August 1827, on the particles contained in the pollen of plants; and on the general existence of active molecules in organic and inorganic bodies". In: *The Philosophical Magazine* 4.21, pp. 161–173.

Burcaw, Lauren M., Els Fieremans, and Dmitry S Novikov (2015). "Mesoscopic structure of neuronal tracts from time-dependent diffusion". In: *NeuroImage* 114, pp. 18–37. ISSN: 10959572. DOI: 10.1016/j.neuroimage.2015.03.061.

Campbell, Graham Robert, Kenneth J Smith, and Don J Mahad (2012). "Mitochondrial changes associated with demyelination: consequences for axonal integrity". In: *Mitochondrial Dysfunction in Neurodegenerative Disorders*. Springer, pp. 175–190.

Clark, CA, GJ Barker, and PS Tofts (1999). "An in vivo evaluation of the effects of local magnetic susceptibility-induced gradients on water diffusion measurements in human brain". In: *Journal of Magnetic Resonance* 141.1, pp. 52–61.

Cleveland, GG et al. (1976). "Nuclear magnetic resonance measurement of skeletal muscle: anisotrophy of the diffusion coefficient of the intracellular water". In: *Biophysical journal* 16.9, pp. 1043–1053.

Concha, Luis et al. (2010). "In vivo diffusion tensor imaging and histopathology of the fimbria-fornix in temporal lobe epilepsy". In: *Journal of Neuroscience* 30.3, pp. 996–1002.

Cook, PA et al. (2006). "Camino: open-source diffusion-MRI reconstruction and processing". In: *14th scientific meeting of the international society for magnetic resonance in medicine*. Vol. 2759. Seattle WA, USA, p. 2759.

Daducci, Alessandro, Erick Jorge Canales-Rodríguez, et al. (2013). "Quantitative comparison of reconstruction methods for intra-voxel fiber recovery from diffusion MRI". In: *IEEE transactions on medical imaging* 33.2, pp. 384–399.

Daducci, Alessandro, Erick J Canales-Rodríguez, et al. (2015). "Accelerated microstructure imaging via convex optimization (AMICO) from diffusion MRI data". In: *Neuroimage* 105, pp. 32–44.

Dhital, Bibek et al. (2019). "Intra-axonal diffusivity in brain white matter". In: *NeuroImage* 189, pp. 543–550.

Dill, Ken and Sarina Bromberg (2012). *Molecular driving forces: statistical thermodynamics in biology, chemistry, physics, and nanoscience*. Garland Science.

Durrieu, J. L., J. Ph Thiran, and F Kelly (2012). "Lower and upper bounds for approximation of the Kullback-Leibler divergence between Gaussian mixture models". In: *ICASSP, IEEE International Conference on Acoustics, Speech and Signal Processing - Proceedings*, pp. 4833–4836. ISBN: 9781467300469. DOI: 10.1109/ICASSP.2012.6289001.

Edelstein, WA, Paul A Bottomley, and Leah M Pfeifer (1984). "A signal-to-noise calibration procedure for NMR imaging systems". In: *Medical Physics* 11.2, pp. 180–185.

Edgar, Julia M and Ian R Griffiths (2014). "White matter structure: a microscopist's view". In: *Diffusion MRI: from quantitative measurement to in vivo neuroanatomy.* Elsevier, pp. 127–154.

Einstein, Albert et al. (1905). "On the motion of small particles suspended in liquids at rest required by the molecular-kinetic theory of heat". In: *Annalen der physik* 17, pp. 549–560.

Ferizi, Uran, Torben Schneider, Eleftheria Panagiotaki, et al. (2014). "A ranking of diffusion MRI compartment models with in vivo human brain data". In: *Magnetic resonance in medicine* 72.6, pp. 1785–1792.

Ferizi, Uran, Torben Schneider, Thomas Witzel, et al. (2015). "White matter compartment models for in vivo diffusion MRI at 300 mT/m". In: *NeuroImage* 118, pp. 468–483.

Filley, Christopher (2012). *The behavioral neurology of white matter*. Oxford University Press.

Filo, Shir and Aviv A Mezer (2018). "PD: Proton Density of Tissue Water 1". In: *Quantitative MRI of the Brain*. CRC Press, pp. 55–72.

Friede, Reinhard L and T Samorajski (1970). "Axon caliber related to neurofilaments and microtubules in sciatic nerve fibers of rats and mice". In: *The Anatomical Record* 167.4, pp. 379–387.

Garrido, Leoncio et al. (1994). "Anisotropy of water diffusion in the myocardium of the rat." In: *Circulation research* 74.5, pp. 789–793.

Gibbs, J Willard (2014). *Elementary principles in statistical mechanics*. Courier Corporation.

Gouw, AA et al. (2008). "Heterogeneity of white matter hyperintensities in Alzheimer's disease: post-mortem quantitative MRI and neuropathology". In: *Brain* 131.12, pp. 3286–3298.

Grover, Vijay PB et al. (2015). "Magnetic resonance imaging: principles and techniques: lessons for clinicians". In: *Journal of clinical and experimental hepatology* 5.3, pp. 246–255.

Hall, Matt G (2016). "Continuity, the Bloch-Torrey equation, and Diffusion MRI". In: *arXiv preprint arXiv:1608.02859*.

Hall, Matt G and Daniel C Alexander (2009). "Convergence and parameter choice for Monte-Carlo simulations of diffusion MRI". In: *IEEE transactions on medical imaging* 28.9, pp. 1354–1364.

Henkelman, R Mark et al. (1994). "Anisotropy of NMR properties of tissues". In: *Magnetic resonance in medicine* 32.5, pp. 592–601.

Herculano-Houzel, Suzana (2009). "The human brain in numbers: a linearly scaled-up primate brain". In: *Frontiers in human neuroscience* 3, p. 31.

Hershey, John R and Peder A Olsen (2007). "Approximating the Kullback Leibler divergence between Gaussian mixture models". In: *ICASSP, IEEE International Conference on Acoustics, Speech and Signal Processing - Proceedings*. Vol. 4. ISBN: 1424407281.

DOI: 10.1109/ICASSP.2007.366913. URL: https://www.researchgate.net/publication/4249249.

Hirano, Asao and Josefina F Llena (2009). "Morphology of central nervous system axons". In: *The axon: structure, function and pathophysiology*. Oxford University Press.

Irimia, Andrei et al. (2012). "Patient-tailored connectomics visualization for the assessment of white matter atrophy in traumatic brain injury". In: *Frontiers in neurology* 3, p. 10.

Jelescu, Ileana O and Matthew D Budde (2017). "Design and validation of diffusion MRI models of white matter". In: *Frontiers in physics* 5, p. 61.

Jelescu, Ileana O, Jelle Veraart, et al. (2016). "Degeneracy in model parameter estimation for multi-compartmental diffusion in neuronal tissue". In: *NMR in Biomedicine* 29.1, pp. 33–47.

Johansen-Berg, Heidi and Timothy EJ Behrens (2013). *Diffusion MRI: from quantitative measurement to in vivo neuroanatomy*. Academic Press.

Jones, Derek K (2010). *Diffusion MRI*. Oxford University Press. ISBN: 0195369777. URL: https://www.amazon.com/Diffusion-MRI-Derek-K-Jones/dp/0195369777?SubscriptionId=AKIAIOBINVZYXZQZ2U3A&tag=chimbori05-20&linkCode=xm2&camp=2025&creative=165953&creativeASIN=0195369777.

Kärger, Jörg and Wilfried Heink (1983). "The propagator representation of molecular transport in microporous crystallites". In: *Journal of Magnetic Resonance (1969)* 51.1, pp. 1–7.

Kasprian, Gregor et al. (2008). "In utero tractography of fetal white matter development". In: *Neuroimage* 43.2, pp. 213–224.

Kiselev, Valerij G (2010). "The cumulant expansion: an overarching mathematical framework for understanding diffusion NMR". In: *Diffusion MRI: theory, methods, and applications*. Oxford University Press, pp. 152–168.

Klawiter, Eric C et al. (2011). "Radial diffusivity predicts demyelination in ex vivo multiple sclerosis spinal cords". In: *Neuroimage* 55.4, pp. 1454–1460.

Klioze, User:Doctor (2013). *MRI: Basic Physics & a Brief History - YouTube*. https://www.youtube.com/watch?v=djAxjtN_7VE. (Accessed on 05/14/2019).

Kolasinski, James et al. (2012). "A combined post-mortem magnetic resonance imaging and quantitative histological study of multiple sclerosis pathology". In: *Brain* 135.10, pp. 2938–2951.

Korkmaz, Selcuk, Dincer Goksuluk, and Gokmen Zararsiz (2014). "MVN: An R package for assessing multivariate normality". In: *The R Journal* 6.2, pp. 151–162.

Kravtsov, VE, IV Lerner, and VI Yudson (1985). "Random walks in media with constrained disorder". In: *Journal of Physics A: Mathematical and General* 18.12, p. L703.

Le Bihan, Denis, Eric Breton, et al. (1986). "MR imaging of intravoxel incoherent motions: application to diffusion and perfusion in neurologic disorders." In: *Radiology* 161.2, pp. 401–407.

Le Bihan, Denis, Cyril Poupon, et al. (2006). "Artifacts and pitfalls in diffusion MRI". In: *Journal of Magnetic Resonance Imaging: An Official Journal of the International Society for Magnetic Resonance in Medicine* 24.3, pp. 478–488.

Lian, J, DS Williams, and IJ Lowe (1994). "Magnetic resonance imaging of diffusion in the presence of background gradients and imaging of background gradients". In: *Journal of Magnetic Resonance, Series A* 106.1, pp. 65–74.

Liewald, Daniel et al. (2014). "Distribution of axon diameters in cortical white matter: an electron-microscopic study on three human brains and a macaque". In: *Biological cybernetics* 108.5, pp. 541–557.

Liu, Chunlei et al. (2011). "High-field (9.4 T) MRI of brain dysmyelination by quantitative mapping of magnetic susceptibility". In: *Neuroimage* 56.3, pp. 930–938.

Lori, Nicolas F, Thomas E Conturo, and Denis Le Bihan (2003). "Definition of displacement probability and diffusion time in q-space magnetic resonance measurements that use finite-duration diffusion-encoding gradients". In: *Journal of Magnetic Resonance* 165.2, pp. 185–195.

McCall, David W, Dean C Douglass, and Ernest W Anderson (1963). "Self-diffusion studies by means of nuclear magnetic resonance spin-echo techniques". In: *Berichte der Bunsengesellschaft für physikalische Chemie* 67.3, pp. 336–340.

McRobbie, Donald W et al. (2017). *MRI from Picture to Proton*. Cambridge university press.

Mitra, Partha P and Bertrand I Halperin (1995). "Effects of finite gradient-pulse widths in pulsed-field-gradient diffusion measurements". In: *Journal of Magnetic Resonance, Series A* 113.1, pp. 94–101.

Moll, Natalia M et al. (2011). "Multiple sclerosis normal-appearing white matter: Pathology–imaging correlations". In: *Annals of neurology* 70.5, pp. 764–773.

Moseley, ME et al. (1990). "Diffusion-weighted MR imaging of acute stroke: correlation with T2-weighted and magnetic susceptibility-enhanced MR imaging in cats." In: *American Journal of Neuroradiology* 11.3, pp. 423–429.

Mottershead, JP et al. (2003). "High field MRI correlates of myelin content and axonal density in multiple sclerosis". In: *Journal of neurology* 250.11, pp. 1293–1301.

Mussel, Matan, Lilah Inzelberg, and Uri Nevo (2017). "Insignificance of active flow for neural diffusion weighted imaging: A negative result". In: *Magnetic resonance in medicine* 78.2, pp. 746–753.

Nixon, Ralph A (1998). "Dynamic behavior and organization of cytoskeletal proteins in neurons: reconciling old and new findings". In: *Bioessays* 20.10, pp. 798–807.

Novikov, Dmitry S, Els Fieremans, et al. (2019). "Quantifying brain microstructure with diffusion MRI: Theory and parameter estimation". In: *NMR in Biomedicine* 32.4, e3998.

Novikov, Dmitry S and Valerij G Kiselev (2010). "Effective medium theory of a diffusion-weighted signal". In: *NMR in Biomedicine* 23.7, pp. 682–697.

Novikov, Dmitry S, Valerij G Kiselev, and Sune N Jespersen (2018). "On modeling". In: *Magnetic resonance in medicine* 79.6, pp. 3172–3193.

Panagiotaki, Eleftheria et al. (2012). "Compartment models of the diffusion MR signal in brain white matter: a taxonomy and comparison". In: *Neuroimage* 59.3, pp. 2241–2254.

Pierpaoli, Carlo et al. (1996). "Diffusion tensor MR imaging of the human brain." In: *Radiology* 201.3, pp. 637–648. ISSN: 0033-8419. DOI: 10.1148/radiology.201.3.8939209. URL: http://pubs.rsna.org/doi/10.1148/radiology.201.3.8939209.

Porras-Cerron, Jaime Carlos (2016). "Comparación de Pruebas de Normalidad Multivariada". In: *Anales Científicos*. Vol. 77. 2. Universidad Nacional Agraria La Molina, pp. 141–146.

Price, William S (1997). "Pulsed-field gradient nuclear magnetic resonance as a tool for studying translational diffusion: Part 1. Basic theory". In: *Concepts in Magnetic Resonance: An Educational Journal* 9.5, pp. 299–336.

Rios-Carrillo, Ricardo Alonso (2017). "Sensado comprimido en imágenes de resonancia magnética pesadas por difusión de agua". MA thesis. Mexico: Centro de Investigación en Matemáticas.

Roos, Nico (2014). "Entropic forces in Brownian motion". In: *American Journal of Physics* 82.12, pp. 1161–1166.

Saksena, Sona et al. (2008). "Diffusion tensor imaging in the developing human cerebellum with histologic correlation". In: *International Journal of Developmental Neuroscience* 26.7, pp. 705–711.

Scherrer, Benoit and Simon K Warfield (2010). "Why multiple b-values are required for multi-tensor models. Evaluation with a constrained log-Euclidean model". In: *2010 IEEE International Symposium on Biomedical Imaging: From Nano to Macro*. IEEE, pp. 1389–1392.

— (2012). "Parametric representation of multiple white matter fascicles from cube and sphere diffusion MRI". In: *PLoS one* 7.11, e48232.

Schmierer, Klaus et al. (2008). "Quantitative magnetic resonance of postmortem multiple sclerosis brain before and after fixation". In: *Magnetic Resonance in Medicine: An Official Journal of the International Society for Magnetic Resonance in Medicine* 59.2, pp. 268–277.

Seewann, Alexandra et al. (2009). "Diffusely abnormal white matter in chronic multiple sclerosis: imaging and histopathologic analysis". In: *Archives of neurology* 66.5, pp. 601–609.

Stejskal, Edward O and John E Tanner (1965). "Spin diffusion measurements: spin echoes in the presence of a time-dependent field gradient". In: *The journal of chemical physics* 42.1, pp. 288–292.

Takahashi, Masaya et al. (2002). "Magnetic resonance microimaging of intraaxonal water diffusion in live excised lamprey spinal cord". In: *Proceedings of the National Academy of Sciences* 99.25, pp. 16192–16196.

Torrey, Henry C (1956). "Bloch equations with diffusion terms". In: *Physical review* 104.3, p. 563.

Trapp, Bruce D and Grahame J Kidd (2004). "Structure of the myelinated axon". In: *Myelin biology and disorders*. Elsevier, pp. 3–27.

Tuch, David S et al. (2002). "High angular resolution diffusion imaging reveals intravoxel white matter fiber heterogeneity". In: *Magnetic Resonance in Medicine: An Official Journal of the International Society for Magnetic Resonance in Medicine* 48.4, pp. 577–582.

Wimberger, Daniela M et al. (1995). "Identification of" premyelination" by diffusion-weighted MRI." In: *Journal of computer assisted tomography* 19.1, pp. 28–33.

Zhu, Xinghua et al. (2013). "Model selection and estimation of multi-compartment models in diffusion MRI with a Rician noise model". In: *International Conference on Information Processing in Medical Imaging*. Springer, pp. 644–655.